JM PAPERS

Momentum transfer across an open-channel, turbulent flow

Predrag Popović[1,2,†], Olivier Devauchelle[1] and Eric Lajeunesse[1]

[1]Institut de Physique du Globe de Paris, F-75238 Paris, France
[2]Faculty of Physics, University of Belgrade, POB 44, 11001 Belgrade, Serbia

The distribution of stress generated by a turbulent flow matters for many natural phenomena, of which rivers are a prime example. Here, we use dimensional analysis to derive a linear, second-order ordinary differential equation for the distribution of stress across a straight, open channel, with an arbitrary cross-sectional shape. We show that this equation is a generic first-order correction to the shallow-water theory in a channel of large aspect ratio. It has two adjustable parameters – the dimensionless diffusion parameter, χ, and a local-shape parameter, α. By assuming that the momentum is carried across the stream primarily by eddies and recirculation cells with a size comparable to the flow depth, we estimate χ to be of the order of the inverse square root of the friction coefficient, $\chi \sim C_f^{-1/2}$, and predict that α vanishes when the flow is highly turbulent. We examine the properties of this equation in detail and confirm its applicability by comparing it with flume experiments and field measurements from the literature. This theory can be a basis for finding the equilibrium shape of turbulent rivers that carry sediment.

Key words: channel flow, turbulence modelling, river dynamics

1. Introduction

Channels whose shape and evolution are determined by the interaction with the flow are common in nature – examples include alluvial rivers (Glover & Florey 1951; Parker 1978*a*), ice streams (Echelmeyer *et al.* 1994) or blood vessels (Rodbard 1975). In alluvial rivers, for example, the sediment is transported by the slight deviations from the threshold stress needed to dislodge a grain from the bed (Parker 1978*b*). The fact that these deviations are small makes the river's shape sensitive to the detailed distribution of the stress across the stream. The problem of estimating stress across a channel is therefore, both important, due to its implications for landscape evolution (Métivier & Barrier 2012), and difficult, since the estimate needs to be accurate (Popović *et al.* 2021).

† Email address for correspondence: arpedjo@gmail.com

When the flow in the channel is steady, the friction on the bottom consumes all of the momentum injected by gravity into the overlying fluid. In the idealised case of a flow over a flat, inclined plane with a slope S, this basic balance requires that the stress, τ, on the channel's bottom be proportional to the flow depth, D. Even when the channel is not completely flat in the cross-stream direction, this proportionality still approximately holds at each point, y, across the stream, provided that the depth, $D(y)$, varies slowly enough with y, i.e.

$$\tau(y) \approx \rho g S D(y), \tag{1.1}$$

where ρ is the fluid density and g is the acceleration due to gravity. This is a simple form of the 'shallow-water' approximation.

The shallow-water theory of (1.1) ignores any transfer of momentum between adjacent fluid columns. Despite its simplicity, it was successfully used to describe the shape of straight, laboratory rivers with a laminar flow that carry no sediment (Seizilles *et al.* 2013). Building on this work, Abramian, Devauchelle & Lajeunesse (2020) performed similar experiments with laminar rivers that carried sediment, while Popović *et al.* (2021) developed a theory to describe the shape of such rivers. The theory of Popović *et al.* (2021) made clear that the shallow-water approximation was not sufficient to describe rivers that carry sediment – the properties of such rivers were critically affected by the transfer of momentum across the stream.

Here, we are mainly motivated by extending the above theory from laminar rivers to natural ones. As a first step towards that end, we investigate the simplest case relevant to this problem – a turbulent flow driven by gravity in a straight, open channel with a fixed cross-section. We aim to find an approximation for the stress, $\tau(y)$, across the bed of such a channel that goes beyond the shallow-water theory, and captures the first-order effects of turbulent momentum transfer. In such a flow, approximations based only on first principles are not available – the flow is unsteady and complicated, as turbulent eddies mix the fluid, and secondary flows organise into recirculation cells (Tominaga *et al.* 1989; Blanckaert, Duarte & Schleiss 2010; Chauvet 2014).

Many models that deal with the turbulent transfer of momentum were developed in the context of flood management (Bousmar & Zech 1999; Martin-Vide & Moreta 2008; Proust *et al.* 2009; Kaddi *et al.* 2022). These models typically split the channel into several regions (such as the deep main channel and the shallow floodplain) and parameterise the interaction between them. However, this splitting does not yield a continuous distribution of the stress, $\tau(y)$, across the channel. Possibly the simplest model that does this was presented in Wark, Samuels & Ervine (1990), and developed earlier in Samuels (1985) starting from the Navier–Stokes equations. There, the shallow-water approximation of (1.1) was supplemented with an empirical term for the turbulent diffusion of momentum, allowing one to calculate the profiles of stress and velocity across the stream, $\tau(y)$ and $U(y)$, by solving an ordinary differential equation (ODE). Similar models, such as that of Shiono & Knight (1991), were developed along the same lines to include additional effects, such as those due to secondary flows.

In this paper we develop a model along similar lines as Wark *et al.* (1990). Our goal is to examine this model in detail, and show that it can be used within a broader theory of river self-organisation. To make clear the assumptions that go into the model, we start from a depth-integrated momentum balance (§ 2), and derive the model from dimensional analysis and symmetry arguments under several broad assumptions about the nature of the turbulent flow, without invoking the Navier–Stokes equations (§ 3). This model corrects the shallow-water theory to first order in a channel with slowly varying bed topography. The distribution of the stress across the stream, $\tau(y)$, in this model is
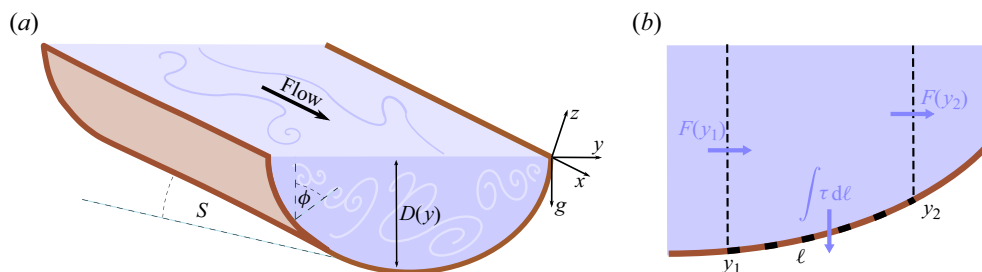
Figure 1. (*a*) Turbulent flow in a straight, open channel. The depth profile, $D(y)$, is constant along the downstream direction, x, and varies along the cross-stream direction, y. At each point across the profile, the normal to the bed makes an angle ϕ with the z axis. The channel makes a constant downstream slope, S, with the horizontal. The upper surface is flat and open. (*b*) Momentum balance in a portion of the channel between coordinates y_1 and y_2. The length of the channel section along the bed is ℓ. Momentum is injected into the section by gravity, and is lost to friction at the bottom. It is transferred across the boundaries at y_1 and y_2 by the flow.

a solution to a second-order linear ODE with two dimensionless parameters (§ 4) – the diffusion parameter for the stress, χ, which controls the magnitude of the cross-stream flux of momentum and the local-shape parameter, α, which controls the effect of the local variations of the channel's shape on the flux. By assuming that the momentum is carried across the stream by the largest eddies and recirculation cells, whose size is comparable to the flow depth and that move at about the frictional velocity, we estimate the orders of magnitude of χ and α. This model predicts a smooth stress distribution across the stream on scales comparable to the flow depth – when there are strong recirculation cells in the flow, the model predicts a reasonable average stress over several such cells, while significant deviations can remain on the scale of an individual cell.

We then proceed to explore this model in the full range of its parameters. Interestingly, we find that fixing the parameters at $\chi = 1/3$ and $\alpha = 1$ approximately describes the stress in a laminar flow, a result that connects natural rivers with small-scale laboratory experiments (§ 4.1). When the flow is turbulent, these parameters can, in principle, take any value, so we investigate how they affect the stress distribution in channels of various shapes, and demonstrate the qualitative effects of the cross-stream transfer of momentum, some of which may have important implications for river formation (§ 5). Finally, we suggest values of the parameters χ and α for practical use. We show that our model with these parameters provides a reasonable agreement with experiments and field data (§ 6). For this reason, and because it is simple and interpretable, it can serve as a basis for a minimal model of self-formed alluvial rivers.

2. Momentum balance

We consider the following problem: a turbulent fluid is driven by gravity down a straight, open channel with a fixed depth profile, $D(y)$, and a downstream slope, S (figure 1*a*). Here, y is the cross-stream coordinate, x is the downstream coordinate and z is the coordinate normal to the free surface of the fluid, which we assume to be flat. The slope, S, is defined as the sine of the angle the channel makes with the horizontal, and is typically small in rivers (10^{-5} to 10^{-2}, Métivier *et al.* 2016). We assume that all properties of the flow are uniform on average in the x direction so that we only need to consider the flow in the (y, z) plane. We attempt to find the time-averaged stress, $\tau(y)$, the fluid exerts at each point across the channel bottom, as well as the lateral profile of the vertically averaged

Symbol	Name	Units	Equation
x, y, z	Downstream, cross-stream, and vertical coordinate	m	
D	Flow depth	m	
τ	Stress on the channel bottom	$\mathrm{kg\,m^{-1}\,s^{-1}}$	
$\tilde{x}, \tilde{y}, \tilde{z}, \tilde{D}, \tilde{\tau}$	Dimensionless coordinates, depth, and stress	None	(4.5a–c)
$\langle \tau \rangle$	Average stress across the entire channel	$\mathrm{kg\,m^{-1}\,s^{-1}}$	
$\langle \tau \rangle_w$	Average stress on the vertical side walls	$\mathrm{kg\,m^{-1}\,s^{-1}}$	(5.1)
F	Cross-stream flux of momentum	$\mathrm{kg\,s^{-1}}$	(3.7) and (4.3)
R_h	Hydraulic radius	m	
Q	Water discharge	$\mathrm{m^3\,s^{-1}}$	
S	Downstream slope	None	
U	Vertically averaged velocity	$\mathrm{m\,s^{-1}}$	
$u(z)$	Vertical profile of downstream velocity	$\mathrm{m\,s^{-1}}$	
U^*	Frictional velocity	$\mathrm{m\,s^{-1}}$	
$\mathcal{D}_e$	Eddy diffusivity	$\mathrm{m^2\,s^{-1}}$	
ν	Molecular diffusivity	$\mathrm{m^2\,s^{-1}}$	
Λ	Diffusion parameter for momentum	None	(3.3)
χ	Diffusion parameter for the stress	None	(4.3)
α	Local-shape parameter	None	(3.5)
θ	Boundary condition on a vertical wall	None	(5.2)
λ	Diffusion length scale	m	(5.4)
φ_w	Fraction of momentum transferred to side walls	None	(5.5)
C_f	Friction coefficient	None	(4.1)
Re	Reynolds number	None	

Table 1. Symbols used throughout the paper.

downstream velocity, $U(y)$. For convenience, we summarise a list of symbols we use throughout the paper in table 1.

We begin by examining the balance of streamwise momentum within a portion of the channel between two vertical slices at locations y_1 and y_2 (figure 1b). Gravity injects momentum into this portion at a rate $\int_{y_1}^{y_2} \rho g S D \, \mathrm{d}y$, where ρ is the fluid density and g is the acceleration due to gravity. The turbulent flow moves momentum in and out of the portion through its vertical sides. In steady state, all the momentum that enters the section is lost to friction along the bed, which occurs at a rate $\int_{\ell} \tau \, \mathrm{d}\ell$, where the integral is performed over the arc, ℓ, of the bed between y_1 and y_2. Altogether, the balance of streamwise momentum for this section of the fluid reads

$$\int_{y_1}^{y_2} \rho g S D \, \mathrm{d}y + F(y_1) - F(y_2) = \int_{\ell} \tau \, \mathrm{d}\ell, \tag{2.1}$$

where F is the flux of momentum across the stream, i.e. the net momentum that crosses a vertical slice of the channel per unit time and length in the streamwise direction (the units of F are $\mathrm{kg\,s^{-2}}$). Bringing y_1 and y_2 infinitesimally close to each other, we find the differential form of this balance:

$$\rho g S D - \frac{\mathrm{d}F}{\mathrm{d}y} = \tau \frac{\mathrm{d}\ell}{\mathrm{d}y}. \tag{2.2}$$

The term $\mathrm{d}\ell/\mathrm{d}y$ is a geometric factor related to the angle, ϕ, between the bed's normal vector and the z axis ($\mathrm{d}\ell/\mathrm{d}y = 1/\cos\phi$). Since the tangent of ϕ equals the local slope of the channel cross-section, $\tan\phi = \mathrm{d}D/\mathrm{d}y$, this term can also be expressed in terms of the

981 A24-4

depth as $\mathrm{d}\ell/\mathrm{d}y = (1 + (\mathrm{d}D/\mathrm{d}y)^2)^{1/2}$. With this, we find the momentum balance equation as

$$\rho gSD - F' - \tau\left(1 + D'^2\right)^{1/2} = 0, \tag{2.3}$$

where the primes stand for derivatives with respect to y. This equation did not require any assumption about the flow – it is equally valid for laminar and turbulent flows.

The specifics of the flow determine how the momentum flux, F, is related to other properties, such as the velocity or the shape of the channel. Ignoring the momentum flux ($F = 0$), and assuming that the bed is nearly flat ($D' \approx 0$), we recover the shallow-water approximation of (1.1):

$$\tau_{sw}(y) = \rho gSD(y), \tag{2.4}$$

where we used the subscript '*sw*' to specifically denote the stress in this approximation. Our goal here is to go beyond this approximation, and estimate F to the lowest non-trivial order, on a variable bed. We do this in the following section.

3. Flux of momentum in a turbulent flow

Due to the complicated nature of turbulent flows, it is challenging to connect the macroscopic properties of the flow, such as the flux of momentum, F, to the Navier–Stokes equations that describe the basic laws of fluid motion (Pope 2011). For this reason, here we develop a simple model for the flux, F, without explicit reference to the Navier–Stokes equations, and confirm it later in § 6 by comparison with measurements. We start by giving examples of physical mechanisms that can give rise to different fluxes (§ 3.1). Afterwards, we use dimensional analysis to mathematically derive a first-order model for the flux on a slowly varying bed under some generic assumptions about the flow (§ 3.2).

3.1. *Physical picture*

Much of the phenomenology of turbulent flows can be derived from the conceptual framework of 'turbulent eddies' that transfer energy from large to small scales through Kolmogorov's energy cascade (Richardson 1920; Prandtl 1925; Taylor 1935). More recently, this physical picture was used to relate the turbulent energy spectrum to macroscopic properties of the flow, such as the vertical velocity profile and the friction coefficient (Gioia & Bombardelli 2001; Gioia & Chakraborty 2006; Gioia *et al.* 2010). If the motion of the eddies is random, they will induce a diffusion of momentum across the stream with a diffusivity, $\mathcal{D}_e$, proportional to their velocity, V, and length scale, L ($\mathcal{D}_e \propto VL$). These eddies mix the fluid from different parts of the flow so that they can generate a flux of momentum, F, across the stream if the downstream velocity, $u(y, z)$, varies throughout the flow, as in figures 2 and 3. In figure 2 the bed is flat ($D' = 0$), the flow is uniform in the vertical ($\partial u/\partial z = 0$), while the depth-averaged velocity, $U(y)$, varies across the stream; in figure 3 the bed has a slope ($D' \neq 0$), the velocity, $u(z)$, varies along the vertical, while its depth average is uniform across the stream ($U' = 0$). We now consider the flux, F, in these two configurations, assuming that the variations of $D(y)$ and $U(y)$ across the stream are slow.

Let us first consider the example of figure 2. In this case, eddies of size L and velocity V carry the downstream momentum across a vertical slice of the channel located at y, mixing the fluid from $y + L/2$ with the fluid from $y - L/2$. The parcels of fluid from $y + L/2$, therefore, carry about $\rho U(y + L/2)$ of momentum and cross the vertical slice in the negative y direction, while those from $y - L/2$ carry about $\rho U(y - L/2)$ of momentum
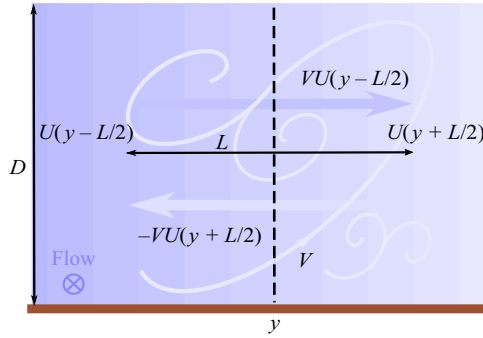
Figure 2. Momentum transfer by large eddies in a flow with a horizontal velocity gradient, U', but a constant vertical velocity profile. This figure shows eddies rotating in the vertical, y–z, plane, but the same analysis applies to those rotating in the horizontal, x–y, plane. Lighter shades of blue indicate faster flow. The largest eddy has a horizontal scale, L, comparable to the depth, D, and a velocity V comparable to the frictional velocity, $U^* = C_f^{1/2} U$. The downstream flow velocity, U, varies slowly in the transverse direction from $U(y - L/2)$ to $U(y + L/2)$ across the scale of the eddy. The eddy mixes the fluid of momentum $\rho U(y - L/2)$ with the fluid of momentum $\rho U(y + L/2)$ across a vertical slice (vertical dashed line). The flux of momentum integrated along this section is proportional to $F \sim \rho DV(U(y - L/2) - U(y + L/2))$ (3.1).
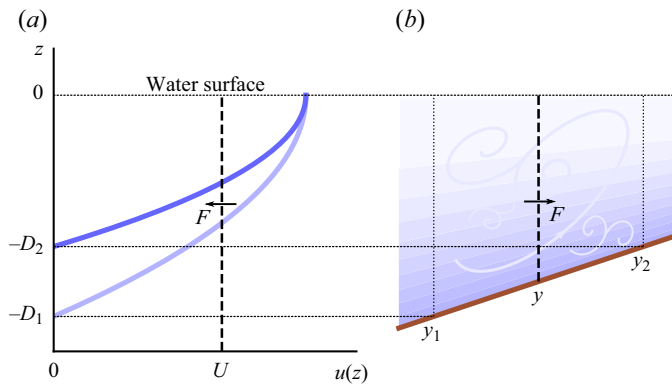

Figure 3. Momentum transfer in a flow with a vertical velocity profile, $u(z)$, and a topography gradient, $D' < 0$, but no horizontal gradient of the depth-averaged velocity, $U' = 0$. (a) Vertical profiles of velocity at two locations across the stream, y_1 and y_2. The profiles are arbitrarily assumed to be quadratic, $u(y, z) = \frac{3}{2} U[1 - z^2/D(y)^2]$. A horizontal velocity gradient develops from the deeper to the shallower part of the flow, inducing a corresponding flux of momentum across the stream, F. (b) Part of the channel corresponding to panel (a). Lighter shades of blue indicate faster flow.

and cross the section in the positive y direction. The flux, F, from these eddies represents the net total amount of momentum that crosses the vertical slice of height D per unit time, so it is about

$$F \sim \rho DV[U(y - L/2) - U(y + L/2)]. \tag{3.1}$$

If the downstream flow velocity, U, varies slowly across the channel, we can approximate the difference in (3.1) as $U(y - L/2) - U(y + L/2) \approx -LU'$, so that the flux generated by these eddies is approximately

$$F \sim \rho DVLU'. \tag{3.2}$$

981 A24-6

Empirically, in wide channels with a rough bottom, eddies reach a size, L, comparable to the flow depth, D, since eddies much larger than this are suppressed by friction at the bottom (Bouchez *et al.* 2010) – it matters little whether these eddies rotate in the vertical, y–z, plane (as in figure 2) or in the horizontal, x–y, plane. According to Kolmogorov's theory, the largest eddies in the flow also move the fastest, so that their diffusivity, $\mathcal{D}_e \propto LV$, is the greatest. We can, therefore, expect that these eddies are responsible for carrying most of the momentum across the stream, and for setting the mixing length (Prandtl 1925). The flux of momentum induced by turbulence scales with the square of the velocity fluctuations (Batchelor 1967), so that the stress, which balances the flux of momentum into the channel's bottom, should scale with the square of the eddy velocity, $\tau \sim \rho V^2$. Therefore, the velocity of the largest eddies should be of the order of the frictional velocity $U^* = \sqrt{\tau/\rho}$. On the other hand, the stress is related to the mean downstream velocity, U, through the empirical friction coefficient, C_f, as $\tau = \rho C_f U^2$. Thus, the velocity, V, of the largest eddies, although much smaller, is proportional to the downstream velocity, $V \sim C_f^{1/2} U$. Using the scalings $L \sim D$ and $V \sim C_f^{1/2} U$ in (3.2), we can write the flux, F, as

$$F \approx -\Lambda \rho C_f^{1/2} D^2 \big(U^2\big)', \tag{3.3}$$

where Λ is a positive, dimensionless number of order one, and the minus sign ensures that the momentum is transferred from fast- to slow-flowing regions. The parameter Λ controls the magnitude of the flux and we call it the dimensionless diffusion parameter.

We now consider the example of figure 3. In this case, a flux of momentum develops across the stream even though the depth-averaged velocity is uniform ($U(y) = $ const.), due to a combination of a sloping bed ($D' \neq 0$) and a variable vertical velocity profile ($\partial u/\partial z \neq 0$). A non-constant vertical profile of velocity means that some eddies will generate a flux of momentum, while the bed slope, $D' \neq 0$, breaks the left–right symmetry and induces a horizontal velocity gradient, $\partial u/\partial y$ (figure 3*a*). If mixing is isotropic, the momentum flux across a vertical slice is proportional to this horizontal gradient, and the total flux, F, scales as $F \sim \rho V \int_{-D}^{0} [\partial u/\partial y]\, \mathrm{d}z$, where V is the velocity of the dominant eddies. Since the horizontal velocity gradient is, in this case, generated by the sloping bed, to first order it scales as $\partial u/\partial y \sim UD'$, and the flux, F, is therefore

$$F \sim \rho VUDD'. \tag{3.4}$$

Using $V \sim C_f^{1/2} U$, we find an approximate expression for the flux in this configuration:

$$F \approx -\alpha \Lambda \rho C_f^{1/2} U^2 \big(D^2\big)'. \tag{3.5}$$

Here α is another dimensionless number of order one, and we keep Λ for later convenience. This flux is proportional to the depth gradient, D', so that it appears to be induced by the bed topography. For this reason, we call α the 'local-shape parameter.' The minus sign in (3.5) means that when α is positive, the flux is generated from the deeper to the shallower parts of the flow. If the vertical profile of velocity, $u(z)$, is top heavy, meaning that the flow is faster near the free surface than at the bottom, a horizontal velocity gradient will indeed develop from deeper to shallower parts of the flow (figure 3). Therefore, positive values of α indicate a top-heavy velocity profile, while α vanishes in the 'plug flow' limit, i.e. when the velocity is constant along the vertical, $u(z) = $ const.

Equations (3.3) and (3.5) for the flux, F, have a similar form, only differing in the position of the cross-stream derivative – in both cases, the flux is proportional to D^2 and to U^2. The term D^2 can be interpreted as a product of the depth, D, of the vertical

slice through which the transfer of momentum occurs and the length scale, L, of the dominant eddies, while the term U^2 can be interpreted as a product of the eddy velocity, V, and the downstream velocity that carries the momentum, U. In agreement with the discussion above, previous experimental studies suggest that the diffusion parameter Λ is of order one. For example, Okoye (1970) showed experimentally that the dimensionless eddy diffusivity, $\mathcal{D}_e/(2C_f^{1/2}UD)$, analogous to our Λ, is of order one, varying between about 0.03 and 1.0. Although we also expect the local-shape parameter, α, to be of order one, it likely vanishes as the flow becomes more and more turbulent, and its velocity profile starts to resemble a vertically uniform 'plug' flow. In Appendix A we estimate the values of Λ and α in a standard model of turbulent diffusion, assuming a logarithmic vertical profile of velocity. There, we find $\Lambda \approx 0.03$, and α vanishing logarithmically with the Reynolds number.

In addition to unsteady eddies, turbulent flows often develop long-lived, coherent secondary currents (Znaien *et al.* 2009; Shih, Hsieh & Goldenfeld 2016). In channel flows with large aspect ratios, these secondary currents form an array of counter-rotating cells that have length scales comparable to the depth, and a transverse velocity of the order of the frictional velocity (Tominaga *et al.* 1989; Blanckaert *et al.* 2010; Chauvet 2014). Therefore, the scalings we introduced previously should still hold for momentum transfer across these cells, even though the momentum transfer on the scale of an individual cell is not diffusive. Thus, if $D(y)$ and $U(y)$ vary slowly over the scale of a single cell, we expect (3.3) and (3.5) to approximately capture the average transfer of momentum smoothed over several cells, although they cannot be accurate at the scale of a single cell.

3.2. *Dimensional analysis*

In the previous section we estimated the flux of momentum, F, in two specific configurations of the flow based on physical reasoning. We now derive a generic, first-order expression for the flux, F, using dimensional analysis. To that end, we make the following broad assumptions about the turbulent flow.

(i) Inertial turbulent regime: Gravity, g, molecular viscosity, ν, and the bed roughness, k_s, do not explicitly change the flux, F. This is certainly not exactly correct – molecular viscosity, ν, and the relative roughness of the bed, k_s/D, both affect the friction coefficient, which can affect the momentum transfer. Nevertheless, we assume that this dependence is weak enough to remove g, ν and k_s from the list of parameters that can affect the flux. We will later relax this assumption by allowing the model parameters to weakly depend on g, ν and k_s.

(ii) Single layer: The depth-averaged downstream velocity, U, is sufficient to characterise the vertical velocity profile of the flow. In other words, we assume that the vertical velocity profile does not change its shape across the stream, so that we do not need to keep track of higher-order moments of the velocity.

(iii) Locality: The flux, F, is locally related to the flow speed and depth. In other words, the flux $F(y)$ is a function of the local depth-averaged velocity, $U(y)$, depth, $D(y)$, and their derivatives up to some finite order, U', D', U'', D'', etc. However, we assume that it does not depend on the far-away parts of the flow (such as a distant wall), nor on the integrated properties of the flow, such as the total flow discharge.

(iv) Slow variation: Finally, we assume that the changes in D and U occur over large scales, so that their higher-order derivatives are much smaller than the lower-order ones, and the flux can be written as an expansion in terms of these derivatives.

This is likely true in a channel with a large aspect ratio. Therefore, we neglect second- and higher-order derivatives when writing a model for F. In this sense, our model is a first-order correction to the shallow-water theory.

Based on the above, our cross-stream flux of momentum, F, can only depend on the fluid density, ρ, the local velocity, $U(y)$, and depth, $D(y)$, as well as their derivatives up to some finite order, U', D', U'', D'', etc. The most general way to construct a quantity with the units of flux (kg s^{-2}) from the quantities above is

$$F = \rho U^2 D \Phi(D', DU'/U, \ldots), \tag{3.6}$$

where Φ is an arbitrary dimensionless function of dimensionless parameters and '$\cdots$' stands for higher-order derivatives written in dimensionless form. This equation states that the dimensionless flux, $F/\rho U^2 D$, can only depend on dimensionless variables, such as D' and DU'/U (Barenblatt 1996). Since we are looking for the lowest-order model for F, we can expand the function Φ as $\Phi \approx c_0 + c_1 D' + c_2 DU'/U + \cdots$, for some constants c_0, c_1 and c_2. However, since the flux is a directed quantity, it should also change sign if we mathematically flip the orientation of the y axis, $F \to -F$ as $y \to -y$. The constant term, c_0, does not obey this symmetry, and, therefore, must vanish. To lowest order, therefore,

$$F \approx -\rho C_f^{1/2} \Lambda \big[D^2 (U^2)' + \alpha U^2 (D^2)' \big], \tag{3.7}$$

where Λ and α are dimensionless numbers. We included the term $C_f^{1/2}$ in the definition of Λ, as in § 3.1, for convenience. Even though we assumed that the flux, F, does not depend on molecular viscosity, bed roughness or the integrated properties of the flow in order to reduce the number of parameters in the dimensional analysis, we can somewhat relax this assumption and allow the constants C_f, Λ and α to weakly depend on these properties, as they likely do.

Equation (3.7) consists of two terms that correspond exactly to (3.3) and (3.5). Although the physical mechanisms we discussed in the previous section are representative of these terms, (3.7) is a generic first-order expression that does not depend on the detailed dynamics of the flow – only the values of the parameters C_f, Λ and α do. If eddies and recirculation cells of a size comparable with the flow depth dominate the momentum transfer, we expect Λ and α to be of order one, with α vanishing in the highly turbulent, 'plug flow' limit (§ 3.1). On the other hand, wide recirculation cells or eddies much larger than the flow depth, cannot be included in our model since they induce a fundamentally non-local flux, violating one of our key assumptions. In Appendix A we show that a standard model of turbulent diffusion satisfies (3.7). In this sense, we may also call (3.7) a diffusive approximation.

Equation (3.7) can also be written in the compact form

$$F = -\rho C_f^{1/2} \Lambda D^{2(1-\alpha)} (D^{2\alpha} U^2)'. \tag{3.8}$$

From here, we can see that the local-shape parameter α determines the part of D^2 inside the derivative. In this way, it controls the quantity that diffuses due to the flux, F – if $\alpha = 0$, it is the depth-averaged velocity, U, while if $\alpha = 1$, it is the depth-integrated momentum, DU.

Wark *et al.* (1990) proposed a model similar to (3.7). However, they do not explicitly include the local-shape parameter, α, but rather mention two alternative models – one in which the velocity, U, diffuses, and another one in which it is the depth-integrated momentum DU ('unit flow' in their terminology). Therefore, they consider two cases

corresponding to $\alpha = 0$ and $\alpha = 1$, and state that it is unclear which one is better. Here we show that these cases are not necessarily special, so that models with non-integer values of α may also be appropriate within the same order of approximation. Besides Wark *et al.* (1990), we are not aware of anyone else who explicitly considered this parameter. Moreover, to our knowledge their model and its consequences have not been carefully examined.

4. Stress on the channel bottom

In the previous section we expressed the cross-stream flux of momentum, F, in terms of the depth, D, and velocity, U (3.7). In this section we show how we can use this result to find the stress, τ, on the channel's bed.

As we mentioned in the previous section, the velocity in a turbulent flow is usually related to the bed stress through the friction coefficient C_f (Chézy 1775),

$$\tau = \rho C_f U^2. \tag{4.1}$$

The friction coefficient depends on the characteristics of the flow, such as the Reynolds number and the bed roughness (Nikuradse 1933). The phenomenological equation of Colebrook (1939) summarises this dependence in circular pipes, and is often used to estimate the friction coefficient in other geometries for which direct measurements are not available. According to this approximation, the friction coefficient can be found as $C_f = f_D/8$, where the Darcy friction factor, f_D, is the solution to

$$\frac{1}{\sqrt{f_D}} = -2\log_{10}\left(\frac{k_s}{3.7R_h} + \frac{2.51}{Re\sqrt{f_D}}\right), \tag{4.2}$$

where $Re = UD/\nu$ is the Reynolds number, $R_h = \mathcal{A}/\mathcal{P}$ is the hydraulic radius of the channel, equal to the ratio of the channel cross-sectional area, $\mathcal{A}$, to its wetted perimeter, $\mathcal{P}$, and k_s is the so-called 'Nikuradse equivalent sand roughness', a parameter that measures the hydraulic roughness of the bed, and vanishes on a smooth bed. The typical values of the friction coefficient, C_f, for experimental flumes and large rivers range between 10^{-3} and 10^{-2} (Lajeunesse, Malverti & Charru 2010a).

Using (4.1) with our expression for the flux (3.7), and assuming the friction coefficient, C_f, is constant across the channel, we find the flux expressed in terms of the stress:

$$F = -\chi\left[D^2\tau' + \alpha(D^2)'\tau\right]. \tag{4.3}$$

Here we introduced the diffusion parameter for the stress, $\chi \equiv \Lambda C_f^{-1/2}$. For the typical values of C_f we mentioned above, we expect this parameter to be about $\chi \sim 10$.

Combining (4.3) with the momentum balance (2.3), and assuming χ is constant across the channel, we find a differential equation for the stress:

$$\chi\left(D^2\tau' + \alpha(D^2)'\tau\right)' - \tau\left(1 + D'^2\right)^{1/2} + \rho g S D = 0. \tag{4.4}$$

For a given depth profile, $D(y)$, and the downstream slope, S, (4.4) is a linear, second-order, ODE for $\tau(y)$. We can further simplify it by rescaling the lengths and stress

981 A24-10

as

$$\tilde{y} = \frac{y}{R_h}, \quad \tilde{D} = \frac{D}{R_h}, \quad \tilde{\tau} = \frac{\tau}{\rho g S R_h}. \tag{4.5a–c}$$

The equation for the stress in terms of these dimensionless variables becomes

$$\chi\big(\tilde{D}^2\tilde{\tau}' + \alpha(\tilde{D}^2)'\tilde{\tau}\big)' - \tilde{\tau}\big(1 + \tilde{D}'^2\big)^{1/2} + \tilde{D} = 0, \tag{4.6}$$

where the primes now stand for derivatives with respect to $\tilde{y}$. This rescaling ensures that the dimensionless stress averages to one over the entire channel ($\langle\tilde{\tau}\rangle = 1$), a result that readily follows from the integrated momentum balance of (2.1).

Equation (4.6) contains two dimensionless parameters – the diffusion parameter for the stress, χ, and the local-shape parameter, α. Converting from dimensionless stress, $\tilde{\tau}(\tilde{y})$, to the physical one, $\tau(y)$, simply requires multiplying by a factor of $\rho g S R_h$. Therefore, for a given channel geometry, the physical stress, τ, depends only on the diffusion parameter, χ, and the local-shape parameter, α, which are set by the details of the flow. Thus, the stress does not depend on the diffusion parameter, Λ, and the friction coefficient, C_f, independently, but only on their combination, $\chi = \Lambda C_f^{-1/2}$.

Instead of writing (4.6) for the stress, we could have equally written an equation for velocity by rewriting $\tilde{\tau} = \tilde{U}^2$, i.e.

$$\chi\big(\tilde{D}^2(\tilde{U}^2)' + \alpha(\tilde{D}^2)'\tilde{U}^2\big)' - \tilde{U}^2(1 + \tilde{D}'^2)^{1/2} + \tilde{D} = 0, \tag{4.7}$$

where $\tilde{U} = U\sqrt{C_f/g S R_h}$ is the dimensionless flow velocity. Wark *et al.* (1990) used precisely this model, although in dimensional form and without explicitly mentioning α. Like the stress, the dimensionless velocity, $\tilde{U}$, is determined by two parameters, χ and α. However, to retrieve the physical velocity, U, we need to multiply $\tilde{U}$ by a factor of $\sqrt{g S R_h/C_f}$, which depends both on the channel geometry (through S and R_h) and on the properties of the flow (through C_f). Although C_f can be estimated using, for example, the Colebrook equation, its value is not certain in channels with irregular geometries, or when roughness is not known. This makes comparing our model with stress measurements more straightforward than comparing it with velocity measurements – to compare with stress, we need to specify two parameters determined by the details of the flow (χ and α), whereas we need to specify three (χ, α and C_f) to compare with velocity. We will, therefore, mostly use the stress equation (4.6), and only refer to the velocity equation (4.7) when needed.

The stress τ that results from (4.6) depends on the entire shape of the channel. In this sense, τ is non-local, even though the flux, F, in (4.3) is locally related to τ and D. In Appendix B we show that when the depth and velocity vary very slowly, or when the diffusion parameter is small, the stress approximately depends only on the local depth of the channel and its derivatives.

4.1. *Connection between turbulent and laminar flows*

How much does a laminar channel flow resemble a turbulent one? Here, we show that there exists a connection between these two cases, at least in the most basic, diffusive approximation we discussed above.
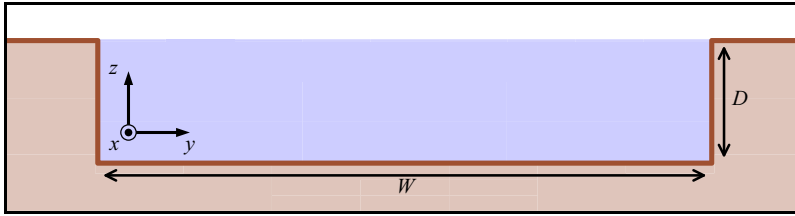
Figure 4. A rectangular channel with an aspect ratio of $W/D = 5$.

Devauchelle, Popović & Lajeunesse (2022) showed that the cross-stream flux of momentum in a straight channel with a laminar flow, F_{lam}, is approximately

$$F_{lam} \approx -\tfrac{1}{3}(D^2 \tau)'. \tag{4.8}$$

This flux has the same form as the turbulent flux in (4.3) with parameters $\chi = 1/3$ and $\alpha = 1$. Therefore, despite the fact that the laminar flux is driven by molecular diffusion while in the turbulent flow, it is driven by diffusion by the largest eddies and recirculation cells, the stress on the bottom of each flow is, to first order, determined by the same (4.4). This similarity may not be all that surprising, since our approximation implicitly assumes a turbulent flux driven simply by gradients of velocity (§ 3.1). However, the above analysis shows that the equivalence between turbulent and laminar flows holds for stress rather than velocity – turbulent and laminar velocities remain different, since they scale differently with the stress.

The transition from the laminar to the turbulent stress can be described by the change in parameters from $\chi = 1/3$ to $\chi \sim 10$ and from $\alpha = 1$ to $\alpha \approx 0$. This result clarifies the extrapolation of the small-scale, laminar rivers to real, turbulent ones (Malverti, Lajeunesse & Métivier 2008; Lajeunesse *et al.* 2010*b*).

5. Analytical solutions in idealised channels

In this section we solve (4.6) in several idealised channels to explore the role of the channel geometry and the effect of the parameters χ and α on the resulting distribution of the stress. This will allow us to bring to light several phenomena that do not exist in the simple shallow-water theory of (1.1), and, therefore, result from the transfer of momentum across the stream.

5.1. *Rectangular channel*

We first consider the case of a rectangular channel with a constant depth, D, and a width, W (figure 4). In this case, the shallow-water theory (1.1) predicts a constant stress on the flat bottom. When the cross-stream flux of momentum exists, however, some of the momentum will be transferred to the vertical side walls, thereby reducing the stress in their vicinity.

In a rectangular channel, (4.4), which assumes that the channel topography varies slowly, becomes ill-defined on the side walls where $D' \to \pm\infty$. Therefore, we cannot hope to find the distribution of the stress along them. However, the model is well defined away from the walls, so that we can still use it on the flat bottom if we take care to specify a boundary condition at the corners where the side walls meet the bottom ($y = \pm W/2$).

This boundary condition is often overlooked in the literature, where it is simply assumed that the velocity, U, vanishes at the corner. Formally, this is true – the velocity of the full Navier–Stokes equations must vanish at all boundaries, so that the proper boundary

981 A24-12

condition is always that of no slip at the side wall. However, for highly turbulent flows, this occurs within a thin viscous boundary layer where the velocity changes very rapidly. At the outer edge of this layer, where the flow becomes properly turbulent, the velocity may be significant. Since we can only hope to apply our model outside of this laminar boundary layer, it may be appropriate to consider a non-vanishing slip velocity at the side walls. Therefore, we will not simply assume the no-slip condition at the side walls, but will, instead, consider a range of possible boundary conditions.

Although we cannot determine the exact distribution of the stress along the side walls, we can find its mean value, $\langle \tau \rangle_w$, from the momentum balance, (2.1). The flux of momentum into the side wall, $F(W/2)$, must be expended by the friction at the wall, so that $F(W/2) = D\langle \tau \rangle_w$. We can, therefore, express the mean side wall stress as

$$\langle \tau \rangle_w = \frac{F(W/2)}{D}, \tag{5.1}$$

which, combined with (4.3) and the fact the bottom is flat ($D' = 0$), yields $\langle \tau \rangle_w = -\chi D \tau'(W/2)$. We use this average stress on the side walls to define the boundary condition at the corner. In particular, we assume that the bottom stress at the corner is some fraction, θ, of the mean side wall stress,

$$\tau(\pm W/2) = \theta \langle \tau \rangle_w. \tag{5.2}$$

This, therefore, defines a mixed boundary condition, wherein the stress at the corner is related to its first derivative, $\tau(W/2) = -\theta \chi D \tau'(W/2)$. We treat θ as an unknown, adjustable parameter of the model.

The parameter α, which controls the importance of topography-induced flux of momentum, becomes irrelevant in a rectangular channel since $D' = 0$ everywhere on the bottom. Therefore, in a rectangular channel the stress is determined by parameters χ and θ rather than χ and α.

The solution of (4.6) in a rectangular channel with the boundary condition (5.2) is

$$\tau(y) = \rho g S D \left(1 - \frac{\cosh(y/\lambda)}{\cosh(W/2\lambda) \left(1 + \theta \sqrt{\chi} \tanh(W/2\lambda) \right)} \right), \tag{5.3}$$

where the diffusion length scale, λ, is given by

$$\lambda \equiv D\sqrt{\chi}. \tag{5.4}$$

In figure 5 we show how the boundary condition, θ, and the diffusion parameter, χ, affect the stress distribution.

The values $\theta = 0$ (figure 5a) and $\theta = 1$ (figure 5b) have a physical interpretation. When $\theta = 0$, the stress at the corner vanishes, $\tau(\pm W/2) = 0$, implying that the depth-averaged velocity in our model also vanishes there, $U(\pm W/2) = 0$ (4.1). This is consistent with a no-slip condition at the side wall ($u(z) = 0$ along the entire side wall). On the other hand, $\theta = 1$ means that the stress at the corner equals the mean stress on the side wall. This has a simple physical interpretation in the limit of large diffusion of momentum, $\chi \to \infty$ – in this limit, $\theta = 1$ means that the stress is distributed uniformly throughout the channel, including on the side walls. For all other values, $\theta \neq 1$, the side walls are not treated equally to the flat bottom when diffusion is high. The fact that the values $\theta = 0$ and $\theta = 1$ are physically significant is the reason we defined the boundary condition through (5.2).

The length scale λ determines how far away from the side walls the flow can feel their presence. More than several λ away from the side walls, the stress approaches the

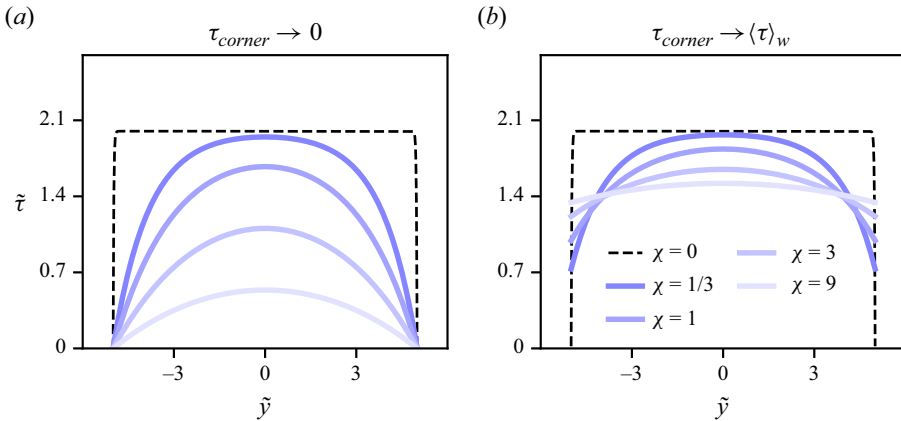

Figure 5. Solutions to (4.6) in the rectangular channel of figure 4 (aspect ratio of $W/D = 5$). Different coloured lines stand for different values of χ (the ratio of the diffusion length to channel width, λ/W, for these solutions varies between 0.11 and 0.6). The black dashed line stands for the shallow-water theory ($\chi = 0$). (a) The stress vanishes at the corner, $\tau(y = \pm W/2) = 0$ ($\theta = 0$). The dark blue line ($\chi = 1/3$ and $\theta = 0$) corresponds to the laminar flow. (b) The stress at the corner equals the mean stress on the side wall, $\tau(y = \pm W/2) = \langle \tau \rangle_w$ ($\theta = 1$).

shallow-water theory, $\tau_{sw} = \rho g S D$. The stress at the centre becomes significantly different from this value when the width is comparable to the diffusion length, $W \sim \lambda$. In other words, the effect of the side walls propagates throughout the entire channel if the aspect ratio of the channel is comparable to the square root of the diffusion parameter for the stress, $W/D \sim \sqrt{\chi}$. For large values of χ (such that $\lambda \gg W$), the stress on the bottom becomes uniform.

To appreciate more clearly the role of the boundary condition parameter, θ, we now show how the stress is partitioned between the bottom and the side walls. Moreover, since this partition is often estimated in experiments, this discussion will be useful for comparison with measurements in § 6. In a rectangular channel, momentum is supplied by gravity at a rate of $\rho g S D W$, and it is transferred partly to the side walls and partly to the channel bottom. The fraction, φ_w, of the total momentum that is transferred to the side walls is, therefore,

$$\varphi_w = \frac{2\langle \tau \rangle_w}{\rho g S W}, \tag{5.5}$$

where $\langle \tau \rangle_w$ is the mean stress on the side walls, and the factor 2 is due to the fact that there are two side walls. Our model predicts φ_w to be ((5.2) and (5.3))

$$\varphi_w = \frac{2D\sqrt{\chi}}{W} \frac{\tanh\left(\dfrac{W}{2D\sqrt{\chi}}\right)}{1 + \theta\sqrt{\chi}\tanh\left(\dfrac{W}{2D\sqrt{\chi}}\right)}. \tag{5.6}$$

In figure 6 we show the fraction, φ_w, as a function of the channel aspect ratio for various values of χ and boundary conditions defined using $\theta = 0$ (figure 6a) and $\theta = 1$ (figure 6b). In the shallow-water theory ($\chi \to 0$), all of the force is carried by the bottom, so $\varphi_w \to 0$.
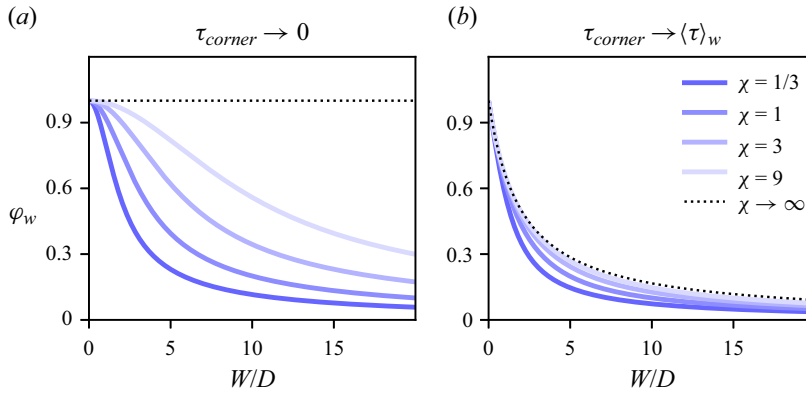
981 A24-14

Figure 6. The fraction of the stress, φ_w, carried by the side walls of a rectangular channel (5.6) as a function of the channel's aspect ratio, W/D, for the case of (a) $\theta = 0$ and (b) $\theta = 1$. Different colours stand for different values of χ. The dark blue line in panel (a) ($\chi = 1/3$ and $\theta = 0$) corresponds to laminar flow. The dotted lines stand for the high-diffusion limit ($\chi \to \infty$, (5.7)).

On the other hand, in the high-diffusion limit ($\chi \to \infty$), this ratio becomes

$$\varphi_w = \frac{1}{1 + \theta \dfrac{W}{2D}}, \quad \chi \to \infty. \tag{5.7}$$

As we mentioned above, when $\theta = 1$, increasing χ uniformises the stress across the entire channel (including the vertical side walls), so that the momentum is transferred to the bottom and to the side walls in proportion to their length, $\varphi_w = 2D/(2D + W)$. On the other hand, a no-slip boundary condition ($\theta = 0$) requires most of the momentum to be transferred to the side walls, so that when $\theta = 0$ and $\chi \to \infty$, the side walls carry all of the stress, $\varphi_w = 1$. In this way, the departure from $\theta = 1$ describes the asymmetry between the bottom and the side walls in the limit of high diffusion. Both $\theta = 0$ (no slip at the side wall) and $\theta = 1$ (uniform stress in the high-diffusion limit) may seem intuitive and we show in § 6 that experimental data are not unanimous about this.

One of the most easily measured quantities is the total water discharge, Q, which we can find in our model as $Q = \int UD \, \mathrm{d}y$. The velocity, U, that follows from (5.3) does not allow us to write this integral in a simple, closed form, so we have to solve it numerically. In figure 7 we show the discharge, Q, normalised by the discharge in the shallow-water theory of (1.1), $Q_{sw} = WD\sqrt{gSD/C_f}$, for $\theta = 0$ and $\theta = 1$ and various values of χ as a function of the channel's aspect ratio. The effect of increasing the diffusion parameter, χ, is quite different for different boundary conditions, $\theta = 0$ and $\theta = 1$. When $\theta = 0$, increasing the diffusion parameter decreases the discharge so that in the limit $\chi \to \infty$ there is no flow (figure 7a). On the other hand, when $\theta = 1$, increasing χ brings the discharge closer and closer to the limit in which the velocity $U = \sqrt{gSR_h/C_f}$ is uniform across the entire channel. In this limit, the discharge is

$$\frac{Q}{Q_{sw}} = \sqrt{\frac{W}{2D + W}}, \quad (\theta = 1, \ \chi \to \infty). \tag{5.8}$$

Therefore, when $\theta = 1$, the discharge curves look alike for any diffusion parameter beyond $\chi \sim 1$ (figure 7b). The transfer of momentum makes the discharge, Q, significantly smaller
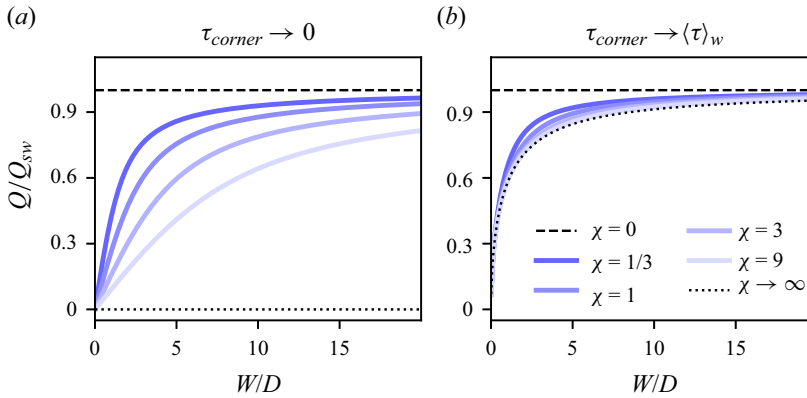
Figure 7. The water discharge, Q, normalised by the shallow-water discharge, $Q_{sw} = WD\sqrt{gSD/C_f}$, in rectangular channels as a function of the channel's aspect ratio, W/D, in the case of (a) $\theta = 0$, and (b) $\theta = 1$. Different colours stand for different values of χ. The black dashed line corresponds to the shallow-water theory ($\chi = 0$), while the black dotted line corresponds to the high-diffusion limit ($\chi \to \infty$, (5.8)).

than the discharge in the shallow-water theory, Q_{sw}, for channels with a small aspect ratio, while, for a large aspect ratio, the shallow-water theory becomes accurate.

Since α does not play a role in a rectangular channel, our model predicts that turbulent and laminar flows lead to the same stress distribution of (5.3) (assuming the same values of χ and θ). In a laminar flow, the velocity must vanish all along the vertical side wall, so the appropriate condition is $\theta = 0$ (no slip), while the diffusion parameter is $\chi = 1/3$ (§ 4.1). The dark blue lines in figures 5(a) and 6(a) show the stress profile and the fraction of the stress carried by the side wall in a laminar flow. Since the relationship between the stress and the velocity is different for laminar and turbulent flows, the discharge, Q, cannot be directly compared between these two cases.

5.2. *Wavy bottom*

In the rectangular channel of the previous section, the stress distribution was independent of the local-shape parameter, α – this parameter only becomes important in channels with variable depth. Here we show that when α is finite, the diffusion of momentum can make the stress higher in shallower parts of the flow. In this way, momentum diffusion can invert one of the most basic predictions of the shallow-water theory, according to which the stress is always greater where the fluid is deeper.

To examine the role of α, we consider an infinitely wide channel with a wavy bottom (figure 8a):

$$D = D_0 + \delta \sin(ky). \tag{5.9}$$

Here D_0 is the mean depth, while k and δ are the wavenumber and the magnitude of the depth perturbation. To first order in small δ/D_0, the solution to our model (4.4) is

$$\tau = \rho g S D_0 \left[1 + \frac{1 - 2\alpha\lambda^2 k^2}{1 + \lambda^2 k^2} \frac{\delta}{D_0} \sin(ky) \right], \tag{5.10}$$

where $\lambda \equiv D_0\sqrt{\chi}$ is the diffusion length scale that we already encountered in the case of rectangular channels (5.4). In figure 8 we show the solutions of (5.10) for $\alpha = 0$ and $\alpha = 1$ and several values of χ.
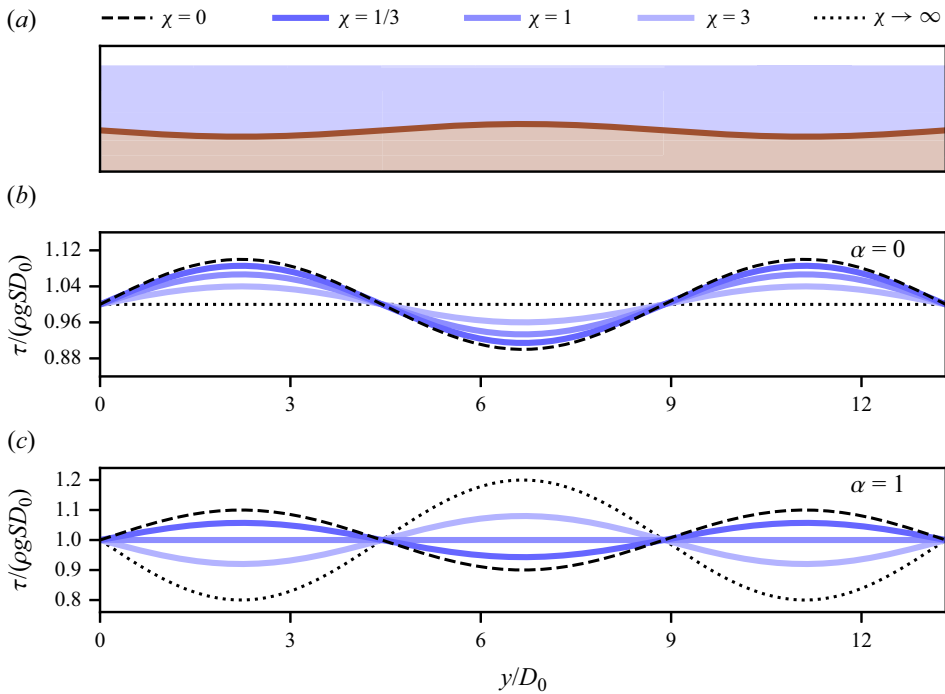
981 A24-16

Figure 8. (*a*) An infinitely wide channel with a wavy bottom (5.9), with $\delta/D_0 = 0.1$ and $D_0 k = 1/\sqrt{2}$. (*b*) Stress distribution of (5.10) with $\alpha = 0$. Different coloured lines stand for different values of χ. The black dashed line stands for the shallow-water theory, $\tau(y) = \rho g S D(y)$ ($\chi = 0$), while the black dotted line stands for the high-diffusion limit ($\chi \to \infty$). (*c*) Stress distribution of (5.10) with $\alpha = 1$. The dark blue curve corresponds to the laminar flow ($\chi = 1/3$ and $\alpha = 1$). The value $\chi = 1$ is the critical value beyond which the stress distribution inverts.

The effect of momentum diffusion depends on the ratio of the diffusion length scale, λ, to the wavelength of the perturbation. When this ratio is small, $\lambda k \ll 1$, we retrieve the shallow-water theory of (1.1). If the wavelength of the perturbation is comparable to the diffusion length scale, the effect of momentum diffusion depends on the value of α. When $\alpha = 0$ (figure 8*b*), momentum diffusion simply reduces the variability of the stress across the channel, so that in the limit of infinite diffusion, $\lambda k \to \infty$, the stress is uniformly spread across the channel and equal to $\rho g S D_0$. Thus, the stress for $\alpha = 0$ is greatest in the deepest parts of the flow, regardless of the strength of momentum diffusion. Conversely, when $\alpha = 1$ (figure 8*c*), there exists a critical bed wavelength below which the stress distribution becomes inverted – the stress becomes highest where the fluid is shallowest. This happens when

$$D_0 k > \frac{1}{\sqrt{2\alpha\chi}}. \tag{5.11}$$

This inversion can occur for any $\alpha > 0$. The limit of infinite diffusion ($\lambda k \to \infty$) in this case does not correspond to a uniformly distributed stress across the channel (black dotted line in figure 8*c*). Instead, it becomes uniform for a finite strength of momentum diffusion, when (5.11) is an equality.

We can understand why this inversion happens by considering the flux written in a compact form, $F = -\chi D^{2(1-\alpha)}(\tau D^{2\alpha})'$ (4.3). The flux tends to homogenise the quantity under the derivative, $\tau D^{2\alpha}$. In the limit of large diffusion, the quantity under the derivative

becomes nearly uniform throughout the channel, $\tau D^{2\alpha} \to$ const., so that the stress scales as $\tau \propto D^{-2\alpha}$. Therefore, when momentum diffusion is strong enough, the stress is inversely proportional to depth for positive values of α. Relating the stress to velocity according to (4.1), this means that when $\alpha > 0$, the fluid may become faster in shallower parts of the flow. Such an inversion of the flow velocity should be readily apparent in an experiment.

The question of this stress inversion is important, since this mechanism may be responsible for setting the instability length scale for braiding rivers (Abramian, Devauchelle & Lajeunesse 2019). This inversion is known to happen in the laminar flow (Devauchelle *et al.* 2022), but it is unclear whether it also happens in turbulent flows. Strictly speaking, our model is only valid when the depth varies slowly, so that its predictions become questionable when $\lambda k \sim 1$. Unfortunately, we were not able to find appropriate experiments in the literature to test this inversion.

5.3. *Triangular channel*

In the previous section we showed that for positive values of α, the stress may become inverted, increasing where the flow is shallower. Here we show that the same mechanism can make the stress in our model diverge at the channel's banks, where the bed intersects the free surface. This divergence suggests that our model fails in such cases, and should therefore be used with care.

We now solve (4.6) in a triangular channel (figure 9a). Although there exist analytical solutions to our model in this configuration, the algebra is too cumbersome to show here. We leave this derivation for Appendix C, and, here, we only discuss the results for $\alpha = 0$ and $\alpha = 1$.

The dimensionless stress profiles, $\tilde{\tau}(\tilde{y})$, are shown in figure 9(b,c). The solutions for $\alpha = 0$ and $\alpha = 1$ look quite different. When $\alpha = 0$, the stress is smooth and reaches a maximum at the centre of the channel. As χ increases, it simply becomes more evenly distributed across the channel. On the other hand, when $\alpha = 1$, the stress reaches a maximum somewhere off-centre and has a kink in the centre. As χ increases in this case, the maximum of the stress moves more and more towards the corners where the flow depth vanishes. When χ reaches a critical value, the stress reaches its maximum at the corners, decreasing linearly towards the centre (light blue line in figure 9c). For even greater values of χ, the stress diverges at the corners, and the theory, therefore, fails. In Appendix C we show that this happens when

$$\left(\frac{D_{max}}{W}\right)^2 > \frac{1 + \sqrt{1 + (4\alpha\chi)^2}}{2(4\alpha\chi)^2}, \qquad (5.12)$$

where D_{max} is the channel depth at its centre and W is the total channel width. This criterion is analogous to (5.11), and the divergence occurs for the same reason as the stress inversion we discussed in § 5.2 – when $\alpha > 0$, a strong diffusion of momentum will make the stress diverge with depth as $\tau \sim D^{-2\alpha}$. Equation (5.12) shows that for any $\alpha > 0$, a steep enough bank angle will cause our theory to fail. Since this divergence does not happen for vanishing α, setting $\alpha = 0$ may be a useful practical choice for modelling purposes.

Laminar flow offers a benchmark for our model since it can be solved without approximation by solving the Poisson equation, $\nabla^2 u = -gS/\nu$ (C.1), and analogies with this equation were sometimes used to estimate the stress in turbulent flows (figure 7.6 in Chow 1959). The divergence of the stress at the banks we discussed does not exist in
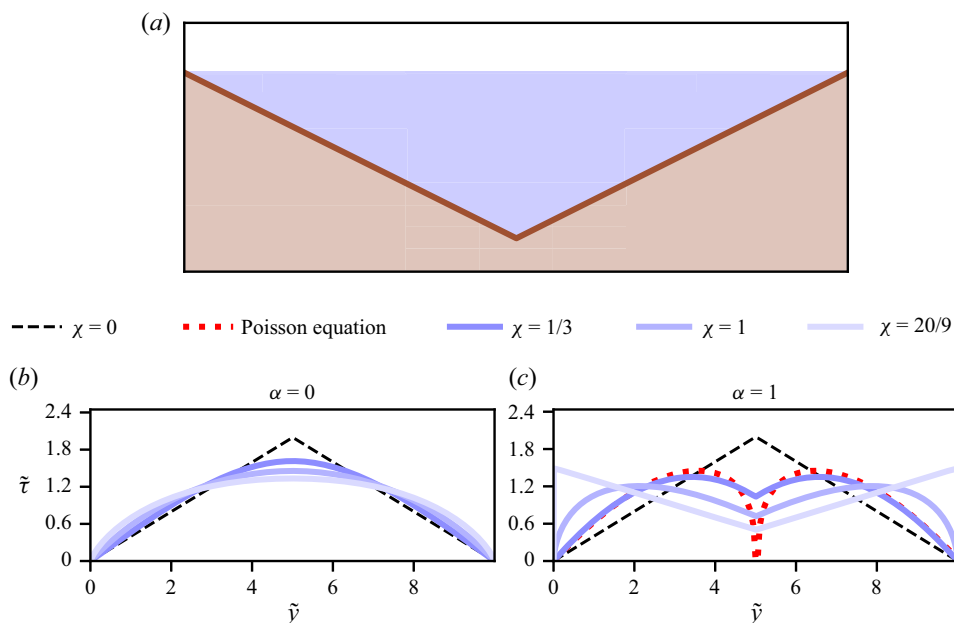
Figure 9. (*a*) A triangular channel with a bank angle of $\phi \approx 27°$. (*b,c*) Dimensionless stress ($\tilde{\tau}$) profiles in our model for different values of χ (different coloured lines) and α. The black dashed line is the shallow-water theory ($\chi = 0$). Panel (*b*) corresponds to $\alpha = 0$, while panel (*c*) corresponds to $\alpha = 1$. The dark blue line in panel (*c*) ($\chi = 1/3$ and $\alpha = 1$) corresponds to the laminar flow in our model, while the red dotted line corresponds to the unapproximated laminar flow. The largest value of χ shown ($\chi = 20/9$) corresponds to the highest value for which the stress in our model does not diverge in the corners of the above channel when $\alpha = 1$ (5.12).

the Poisson equation. Still, in the triangular channel of figure 9, the solution to the Poisson equation closely matches our model with $\chi = 1/3$ and $\alpha = 1$, except near the sharp corner at the centre (red dotted line in figure 9*c*), where the symmetries of the Poisson equation require the stress to rapidly vanish (as in all sharp corners). Although our model is not well suited to treat the flow around such sharp corners, it nonetheless makes a sharp dip at the centre, correctly capturing the trend of the exact solution. We can conclude that even when the bed topography varies quickly, our model predictions should not be disregarded altogether, although one should be careful when using them.

5.4. *Variable roughness*

So far, we assumed that the friction coefficient, C_f, is constant. However, when the roughness of the bed varies across the stream, the diffusion of momentum induces a phenomenon that does not exist in the shallow-water theory – the stress concentrates on the rough parts of the channel (figure 10*a*).

In the shallow-water theory (1.1), the stress at each point simply balances the input of momentum by gravity in the overlying fluid column, so that variations of the channel roughness do not affect the stress. On the other hand, the roughness affects the velocity through the friction coefficient, C_f, so that the flow is slower over the rough parts of the channel (4.1). Therefore, a gradient of velocity develops from the smooth to the rough parts, even in the shallow-water theory. A flux of momentum, F, will thus develop from
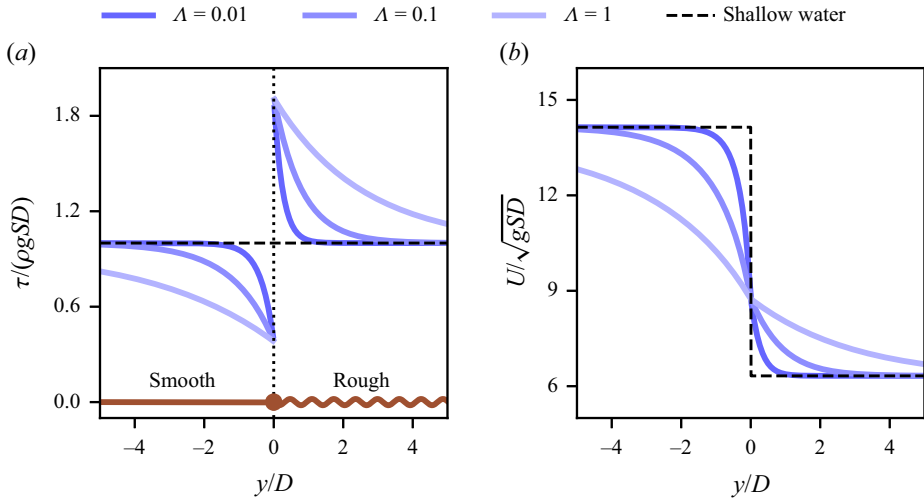
Figure 10. Solutions to (5.13) on a flat bed with variable roughness – the left half ($\tilde{y} < 0$) is smooth, while the right half ($\tilde{y} > 0$) is rough (brown line in panel *a*). We are assuming that C_f adjusts instantaneously to bed roughness, so that it is constant in two halves of the channel, with $C_{f,rough}/C_{f,smooth} = 5$. We are assuming a constant diffusion parameter, Λ. Different blue lines correspond to different values of Λ (the diffusion length scale on the rough side varies between $\lambda/D \approx 0.25$ for the dark blue curve and $\lambda/D \approx 2.5$ for the light blue curve). The black dashed line corresponds to the shallow-water theory. (*a*) Dimensionless stress, $\tau/\rho g S D$. (*b*) Dimensionless velocity, $U/\sqrt{gSD}$.

the smooth to the rough parts of the channel, increasing the stress over the rough and decreasing it over the smooth parts.

Although the friction coefficient, C_f, is in reality determined by the details of the flow, for simplicity, here we assume that it is simply a function of the local bed roughness. Accordingly, when the roughness changes discontinuously, the stress on the bottom can also become discontinuous. However, the velocity, U, will remain continuous. To emphasise the fact that we are looking for a continuous velocity when the roughness varies across the stream, we solve our model in terms of U,

$$\left(\Lambda C_f^{1/2}\left(D^2(U^2)' + \alpha U^2(D^2)'\right)\right)' - C_f U^2(1 + D'^2)^{1/2} + gSD = 0, \qquad (5.13)$$

where we keep the diffusion parameter, Λ (3.7), inside the derivative, since it may also vary. We note that, when the friction coefficient, C_f, varies across the stream, it is not possible to collect Λ and C_f into a single parameter, χ, by rewriting the momentum balance in terms of the stress, τ (even if Λ is constant).

In figure 10 we show a solution to (5.13) on a flat bed on which the roughness suddenly changes (assuming a constant diffusion parameter, Λ). The stress develops a discontinuity at the point where the smooth and the rough parts meet (figure 10*a*). Over the rough part, there is an excess of stress compared with the shallow-water theory, while over the smooth part there is a deficit of stress. In both regions, away from the discontinuity, the stress relaxes exponentially to the shallow-water theory, $\tau_{sw} = \rho g S D$, over the diffusion length scale $\lambda = D\sqrt{\Lambda C_f^{-1/2}}$ (the same one as in (5.4)). The magnitude of the discontinuity does not depend on the value of the diffusion parameter, Λ – around the junction, any amount of momentum diffusion will uniformise the velocity, thereby creating a jump in the stress on the rough part and a dip in the smooth part. The ratio of the stresses on two sides of the junction equals the ratio of the friction coefficients,

981 A24-20

	χ	Λ	α	θ (Seine)	θ (experiments)
Laminar flow	1/3	None	1	0	0
Turbulent flow	$\Lambda C_f^{-1/2}$	0.3	0	0	0.8
	(1.3, 23.4)	(0.07, 1.05)	(−0.1, 0.1)	(0, 0.1)	(0.6, 1)

Table 2. Default model parameters. The values for the laminar flow correspond to the approximation of Devauchelle *et al.* (2022) (§ 4.1), while we suggest a default value (top number) and the uncertainty (brackets) for each turbulent flow parameter based on comparison with the data in § 6. The uncertainty range for Λ roughly corresponds to range of best-fit values to all the experiments of § 6. The default Λ is about the geometric mean of the minimum and the maximum best-fit value. For the laminar flow, Λ is not defined since χ is not related to the friction coefficient, C_f, as in the turbulent case. The value for α is based on comparisons with the floodplain experiments of Shiono & Knight (1991) (§ 6.3). Since the data are inconclusive, we give two values for the boundary condition, θ, for the rectangular channel flow – one based on the comparison with the Seine river (§ 6.1) and another based on the comparison with the flume experiments (§ 6.2). For the laminar flow, $\theta = 0$ always.

$\tau_{rough}/\tau_{smooth} = C_{f,rough}/C_{f,smooth}$. The excess of stress in the rough region creates an excess of force, $\Delta \mathcal{F} = \int_0^\infty (\tau - \tau_{sw})\,\mathrm{d}y = \Delta\tau\lambda$, where $\Delta\tau = \tau_{rough} - \tau_{sw}$ is the deviation from the shallow-water theory at the junction point. This excess of force is proportional to the diffusion length scale, λ. Strong cross-stream diffusion of momentum, therefore, makes the flow pull significantly more on the rough parts of the channel, an effect that the shallow-water theory cannot account for.

The velocity, U, continuously decreases from the smooth to the rough region over the same length scale, λ (figure 10*b*). The gradient in velocity, therefore, creates a flux of momentum from the smooth region to the rough one. In the shallow-water theory, this decrease in U is discontinuous.

6. Comparison with experiments

We now test the predictions of the previous sections by comparing our model, (4.6), against various measurements of stress and velocity in straight channels with a turbulent flow. In table 2 we summarise the values of our model parameters (χ, Λ, α and θ) that best fit these data. In the figures below, we show our model solutions using the default parameters from table 2 – $\chi = \Lambda C_f^{-1/2}$, $\Lambda = 0.3$, $\alpha = 0$ and $\theta = 0$ (for the Seine river) or $\theta = 0.8$ (for the rectangular channel experiments). We chose these default parameters from the range of best-fit values to conveniently represent all of the experiments – our model with the default parameters of table 2 reproduces all of the measurements to within about 30 %.

We start by discussing the Seine river measurements of Chauvet *et al.* (2014) and the rectangular channel experiments reported in Knight, Demetriou & Hamed (1984). Then, we consider the more complicated 'floodplain' geometry of Shiono & Knight (1991). Finally, we discuss the experiments of Blanckaert *et al.* (2010) with variable roughness. We give additional experimental details in Appendix D.

6.1. *The Seine river*

We begin by comparing (5.3) with velocity measurements of Chauvet *et al.* (2014) in the Seine river in Paris, France (figure 11*a*). In order to make the river navigable throughout the year, the banks of the Seine were paved into vertical walls where it crosses Paris. The river flows over bedrock, which is virtually flat. Therefore, the channel of the Seine
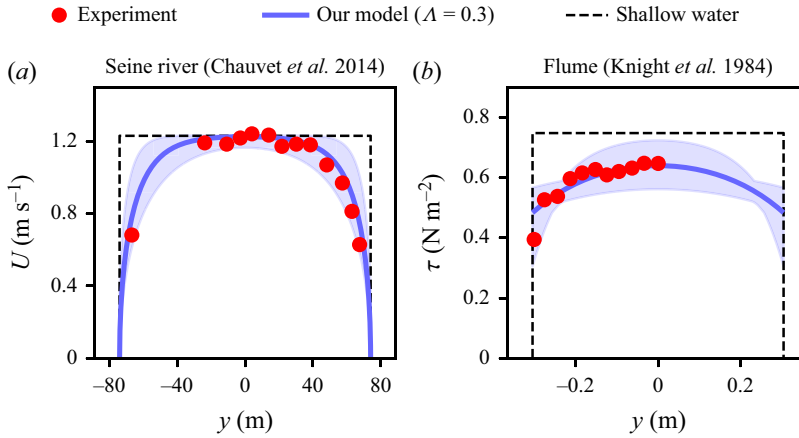
Figure 11. Comparison with measurements in rectangular channels. The red dots represent measurements. The blue lines represent our model with the default values of model parameters from table 2 ($\chi = \Lambda C_f^{-1/2}$ with $\Lambda = 0.3$; since the bottom is flat, the value of the local-shape parameter, α, is irrelevant). The blue shaded area corresponds to the uncertainty in Λ and θ from table 2. The black dashed lines represent the shallow-water theory. (*a*) Measurements of the depth-averaged downstream velocity, U, in the Seine river by Chauvet *et al.* (2014). We show our solution with $C_f = 4 \times 10^{-3}$ and the default $\theta = 0$ (table 2). (*b*) Measurements by Knight *et al.* (1984) of the stress, τ, in a rectangular flume with an aspect ratio of 7.73. We estimate $C_f \approx 2.8 \times 10^{-3}$ from measurements of channel-averaged velocity and stress, and use the default $\theta = 0.8$ (table 2).

is nearly rectangular with an aspect ratio of about 23.9. We give the details about the geometry of the Seine at the time and the location of the measurements in Appendix D.1.

In order to find the velocity, U, in our model we need to specify three parameters – the friction coefficient, C_f, the diffusion parameter for the stress, χ, and the boundary condition, θ. Allowing all these parameters to adjust, we find the best fit for $C_f \approx 4.0 \pm 0.2 \times 10^{-3}$, $\chi = 6.6 \pm 2.5$ ($\Lambda = 0.42 \pm 0.15$) and $\theta \approx -0.03 \pm 0.03$ (we estimate the uncertainty by bootstrapping). Our model with these best-fit parameters matches closely the measurements – the largest error is about 3 % of the mean velocity. In figure 11(*a*) we show that our model with the default parameters of table 2 ($\chi = \Lambda C_f^{-1/2}$, $C_f \approx 4 \times 10^{-3}$, $\Lambda = 0.3$ and $\theta = 0$) also reproduces the data well – maximum error is about 11 % of the mean velocity.

Consistent with our discussion above, the measurements on the Seine suggest a Λ of order one. The best-fit value of C_f is also reasonable – Chézy (1775) estimated it to be about $C_f \approx 5 \times 10^{-3}$, while the Colebrook equation (4.2) yields our best-fit value assuming an equivalent sand roughness, k_s, of the order of several centimetres, a sensible value for the Seine. The measurements above suggest a no-slip condition at the side walls, which, in our model, translates to a vanishing stress at the corners ($\theta \approx 0$).

6.2. *Rectangular flumes*

Next, we turn our attention to the experiments of Knight *et al.* (1984) who measured the distribution of the stress across smooth rectangular channels with varying aspect ratios and Reynolds numbers. We provide more details about their experiments in Appendix D.2.

In figure 11(*b*) we show an example of their measurements of the stress, τ, in a single channel, and compare them to our model. Since the stress rather than velocity is measured, we do not need to specify the friction coefficient, C_f (§ 4) – our model for
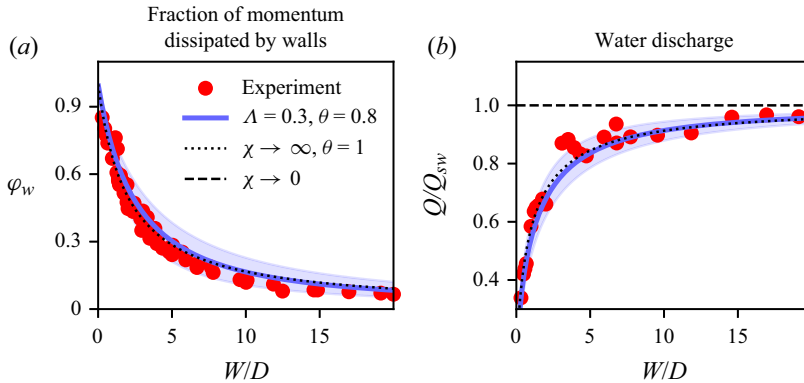
Figure 12. (*a*) The fraction of momentum transferred to channel side walls, φ_w (5.6), and (*b*) the normalised water discharge, Q/Q_{sw}, as a function of the aspect ratio. We assume the friction coefficient $C_f = 2.8 \times 10^{-3}$, as in figure 11(*b*). The blue lines correspond to our model with default parameters of table 2 ($\Lambda = 0.3$ and $\theta = 0.8$), while the blue shaded area corresponds to the uncertainty in these parameters. The red dots in panel (*a*) represent a collection of 60 experiments by various authors reported in Knight *et al.* (1984), while the red dots in panel (*b*) represent 25 experiments performed by Knight *et al.* (1984) themselves. The black dotted lines correspond to a uniform stress across the entire channel ($\chi \to \infty$ and $\theta = 1$, (5.7) and (5.8)). The horizontal black dashed line in panel (*b*) corresponds to the shallow-water prediction, $Q = Q_{sw}$.

τ in a rectangular channel is fully determined by specifying χ and θ. Nevertheless, in order to use our scaling, $\chi = \Lambda C_f^{-1/2}$, we estimate C_f using the reported measurements of the channel-averaged velocity, $\langle U \rangle$, and the mean stress, $\langle \tau \rangle$, as $C_f = \langle \tau \rangle / \rho \langle U \rangle^2$. For the experiment in figure 11(*b*), this yields $C_f \approx 2.8 \times 10^{-3}$, a value consistent with an estimate based on the Colebrook equation (4.2) assuming a smooth channel with a Reynolds number $Re = \langle U \rangle D / \nu$. Allowing Λ and θ to adjust, we find the best fit with $\Lambda = 0.22 \pm 0.05$ and $\theta = 0.73 \pm 0.1$ (for other experiments reported in Knight *et al.* (1984), the best-fit Λ ranges from 0.07 ± 0.01 to 0.22 ± 0.05, and the best-fit θ from 0.7 ± 0.08 to 0.85 ± 0.15). These best-fit solutions reproduce the measurements very well – the error is at most 9 % of the average stress (for other experiments, it is between 5 % and 9 %). In figure 11(*b*) we show that our default solution ($\Lambda = 0.3$ and $\theta = 0.8$) also captures the data well (maximum error is about 16 % of the mean stress).

Knight *et al.* (1984) reported the fraction of momentum transferred to the side walls, φ_w, for each of their 25 experiments and compared it with 35 other experiments performed in smooth rectangular flumes in studies by Cruff (1965), Ghosh & Roy (1970), Kartha & Leutheusser (1970), Knight & Macdonald (1979), Myers (1978) and Noutsopoulos & Hadjipanos (1982). The fraction φ_w for all of these studies approximately falls onto a single curve as a function of the channel's aspect ratio (figure 12*a*). Allowing Λ and θ to vary, we find the best fit with $\Lambda \approx 0.14 \pm 0.07$ and $\theta \approx 0.88 \pm 0.1$, which reproduces the data well (the mean error is about 2 %). The blue line in figure 12(*a*) shows that our model with default parameters ($\Lambda = 0.3$ and $\theta = 0.8$) also falls close to the measurements (the mean error is about 4 %). Moreover, the limit of uniform stress across the channel ($\chi \to \infty$ and $\theta = 1$, (5.7)) also explains the data well (black dotted line in figure 12*a*). In fact, the data for φ_w are consistent with our model for any $\theta \sim 1$, and χ greater than about $\chi \sim 1$.

Although we find good agreement between predicted and measured stress in all of the experiments, measuring stress directly is difficult. For this reason, we also test our model against the measurements of water discharge, a quantity that is easy to measure. In figure 12(*b*) we show that normalising the water discharge, Q, by its value in the

shallow-water theory, $Q_{sw} = U_{sw}DW$, where $U_{sw} = \sqrt{gSD/C_f}$, collapses all of the data points of Knight *et al.* (1984) onto a single curve as a function of the channel aspect ratio. Here, we assumed that $C_f = 2.8 \times 10^{-3}$, the same as in the experiment of figure 11(*b*). Allowing Λ and θ to vary, we find the best fit with $\Lambda = 0.06 \pm 0.03$ and $\theta = 0.8 \pm 0.1$ that reproduces the data with at most 7 % error. Figure 12(*b*) shows that our default model ($\Lambda = 0.3$ and $\theta = 0.8$) also reproduces the data well (maximum error is 11 %). Again, the data are consistent with the limit of uniform stress ($\chi \to \infty$ and $\theta = 1$, (5.8)), so that our model with any $\theta \sim 1$ and $\chi \gtrsim 1$ is compatible with the measurements. Unlike φ_w, which is a statement about the stress, the water discharge is a statement about velocities. Figure 12(*b*), therefore, suggests that the velocity is close to uniform across the channel.

Although Λ in these experiments is smaller than in the Seine (the best fits range from 0.07 to 0.22), it is still of order one, and our default value ($\Lambda = 0.3$) still explains the data well. However, all of the experiments above strongly suggest a boundary condition specified through θ of order one, in stark contrast with the no-slip condition we found for the Seine (§ 6.1). At this point, it is unclear why this difference exists.

6.3. *Floodplain*

The experiments presented above did not allow us to constrain the local-shape parameter, α. To do this, we now consider the flow in a channel with variable depth across the stream. We are unaware of any experiments in the literature that were performed in channels with slowly varying bottom topography and no sharp corners, which would conform with our model's assumptions, and would, therefore, be ideal for this study. However, many previous studies considered the flow in the so-called floodplain geometry (figure 13*a*). Such a configuration was designed to mimic the flow in rivers during flooding, and consists of a deep and relatively narrow main channel joined with a wide and shallow 'floodplain'. Although many models were developed that accurately estimate the stage-discharge relations in this geometry, i.e. how the water level varies with total water discharge (Bousmar & Zech 1999; Martin-Vide & Moreta 2008; Proust *et al.* 2009; Kaddi *et al.* 2022), they typically paid little attention to the detailed distribution of the stress across the banks between the main channel and the floodplain. Yet, in this geometry, our parameter α only plays a direct role on these banks, so, unlike most previous studies, we pay special attention to this transitional region between the main channel and the floodplain.

Here we consider the experiments of Shiono & Knight (1991) in a symmetric floodplain channel (figure 13*a*). The water level changed from one experiment to the next, so that the flow depth in the main channel, D_{mc}, and in the floodplain, D_{fp}, varied. The main channel and the floodplain were connected by banks of unit slope ($D' = \pm 1$), and the floodplain was connected to the water surface by banks of the same slope. In this channel, Shiono & Knight (1991) measured both the stress, $\tau(y)$ (figure 13*b*), and the depth-averaged velocity, $U(y)$ (figure 13*c*), using independent methods (Appendix D.3). We note that bank slopes of $D' = \pm 1$ are not really small so that we consider these experiments only because we lack a more appropriate alternative.

We start by considering the friction coefficient, C_f. Since the Reynolds number is larger in the deep main channel than in the shallow floodplain, C_f is lower in the main channel than in the floodplain. We can estimate the friction coefficient at each point across the stream directly from the measurements of the stress and velocity as $C_f(y) = \tau(y)/\rho U^2(y)$ (figure 13*d*). We find that $C_f \approx 2 \times 10^{-3}$ in the main channel for all experiments, while it varies in the floodplain from one experiment to the other. This variability of C_f across the stream is well captured by the Colebrook equation (4.2) assuming a smooth channel
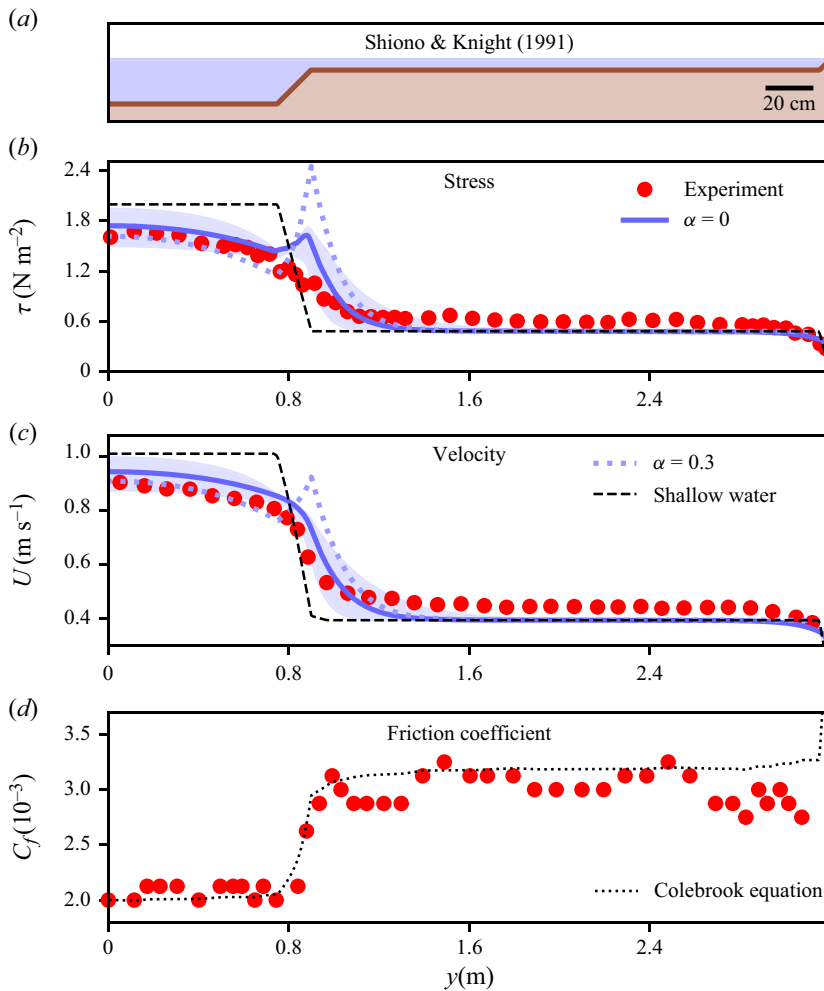
Figure 13. (*a*) Cross-section of one half of the symmetric 'floodplain' channel used by Shiono & Knight (1991) with the depths of the main channel and the floodplain $D_{mc} \approx 19.8$ cm and $D_{fp} \approx 4.8$ cm. (*b*) Measurements (red circles) of the stress, τ, in the channel above. The solid blue line is the solution to (5.13) assuming $\alpha = 0$, $\Lambda = 0.3$ and C_f estimated from the Colebrook equation using an approximated Reynolds number $Re(y) = U_{sw}(y)D(y)/\nu$, where $U_{sw}(y) = \sqrt{gSD(y)/C_{f,def}}$ and $C_{f,def} = 2 \times 10^{-3}$. The blue shading corresponds to uncertainty in Λ from table 2. The blue dotted line corresponds to $\alpha = 0.3$ and $\Lambda = 0.3$. The black dashed line is the shallow-water prediction. (*c*) The depth-averaged velocity, U, with the same notation as in panel (*b*). (*d*) Estimates of the friction coefficient, C_f. The red circles are estimates using the stress and velocity measurements, $C_f(y) = \tau(y)/\rho U^2(y)$. The black dotted line is the estimate based on the Colebrook equation (4.2) assuming a smooth channel and a local Reynolds number, $Re(y) = U(y)D(y)/\nu$. This equation predicts a higher friction coefficient in the floodplain, where the Reynolds number is lower, and a divergence near the right corner of the channel where the Reynolds number vanishes.

($k_s/D = 0$), and a local Reynolds number, $Re(y) = U(y)D(y)/\nu$ (black dotted line in figure 13*d*).

To compute the stress, τ, and the velocity, U, from our model when the friction coefficient varies across the stream, we need to solve (5.13). We supply our model with the friction coefficient $C_f(y)$ estimated using the Colebrook equation with a local Reynolds number $Re(y) = U_{sw}(y)D(y)/\nu$, where $U_{sw}(y) = \sqrt{gSD(y)/C_{f,def}}$ is the shallow-water

velocity and $C_{f,def} = 2 \times 10^{-3}$ is a default friction coefficient that we take to be that of the main channel. This rough estimate of the Reynolds number is sufficient, since C_f in the Colebrook equation depends only weakly on the Reynolds number – using twice the value of $C_{f,def}$, the Colebrook equation yields only about 9 % higher C_f in the floodplain, which corresponds to a floodplain velocity only about 4 % smaller (and similarly in the main channel). Finally, we assume that the parameters Λ and α are constant. Therefore, besides the depth profile, $D(y)$, our model in this case requires three parameters – $C_{f,def}$, Λ and α.

The solutions to our model here are not as accurate as in the rectangular channels of the previous two sections. For this reason, it is not clear how to define the best fit to the data – we may accurately reproduce the data in the main channel, in the floodplain or in the transition region, but not all three at the same time (focusing only on the main channel yields the best-fit Λ from $\Lambda \approx 0.48$ to $\Lambda \approx 1.05$ depending on the experiment, regardless of α). Therefore, we do not attempt to show the best-fit solutions, and, instead, we simply compare our model with the default diffusion parameter ($\Lambda = 0.3$) and two different values of α: $\alpha = 0$ and $\alpha = 0.3$ (figure 13*b*,*c*).

In the main channel and the floodplain, the solutions with $\alpha = 0$ and $\alpha = 0.3$ behave very similarly and reproduce the data equally well. The two solutions differ significantly only in the transition region. They both show a peak in the stress that is not observed in the data, but this peak is more pronounced for $\alpha = 0.3$. When $\alpha = 0$, this peak is caused by the rapidly changing friction coefficient in the transition region, while for $\alpha > 0$, it is caused by the bed topography itself, and would remain even for a constant friction coefficient. Using a negative α could remove this peak of the stress, but would, at the same time, make the stress change more abruptly from the main channel to the floodplain, unlike what we see in the data. The solution with $\alpha = 0$ shows no peak in the velocity, consistent with the measurements, while $\alpha = 0.3$ still shows a small peak. For these reasons, our model conforms with the data only for small (positive or negative) values of α, so, for simplicity, we set $\alpha = 0$ as our default parameter.

In the floodplain, our solution quickly converges to the shallow-water prediction, while the measured stress and velocity remain about 20 % above it – a modest difference that our model cannot account for. This discrepancy can either be the result of a slight bias in the measurements, or, as suggested by Shiono & Knight (1991), caused by a real feature of the flow such as a wide recirculation cell that spans the floodplain or large eddies that exist in the horizontal *x*–*z* plane. These features, which are normally suppressed by the bottom friction in rivers, may play a significant role in smooth channels such as this one.

6.4. *Variable roughness*

Finally, we test the predictions of § 5.4 for a bed with variable roughness by comparing our model with the experiments of Blanckaert *et al.* (2010). They performed high-precision measurements of velocity in half-trapezoidal channels (figure 14*a*) in which the bottom of the channel had a fixed roughness while the right, sloping bank was either smoother, as rough, or rougher than the bottom. They report $C_f \approx 5.3 \times 10^{-3}$ for the bottom based on direct measurements of stress and velocity, and we use the Colebrook equation to estimate $C_f \approx 2.4 \times 10^{-3}$ for the deepest part of the smooth bank and $C_f \approx 1.9 \times 10^{-2}$ for the deepest part of the rough bank (on the sloping bank, C_f increases as the bank becomes shallower). We give the details of these experiments in Appendix D.4.

We show the estimates of Blanckaert *et al.* (2010) for the stress in figure 14(*b*,*c*). As predicted in § 5.4, the stress develops a discontinuity at the junction between the bed and the banks. If the bank is smoother than the flat bottom, the stress on the bank suddenly
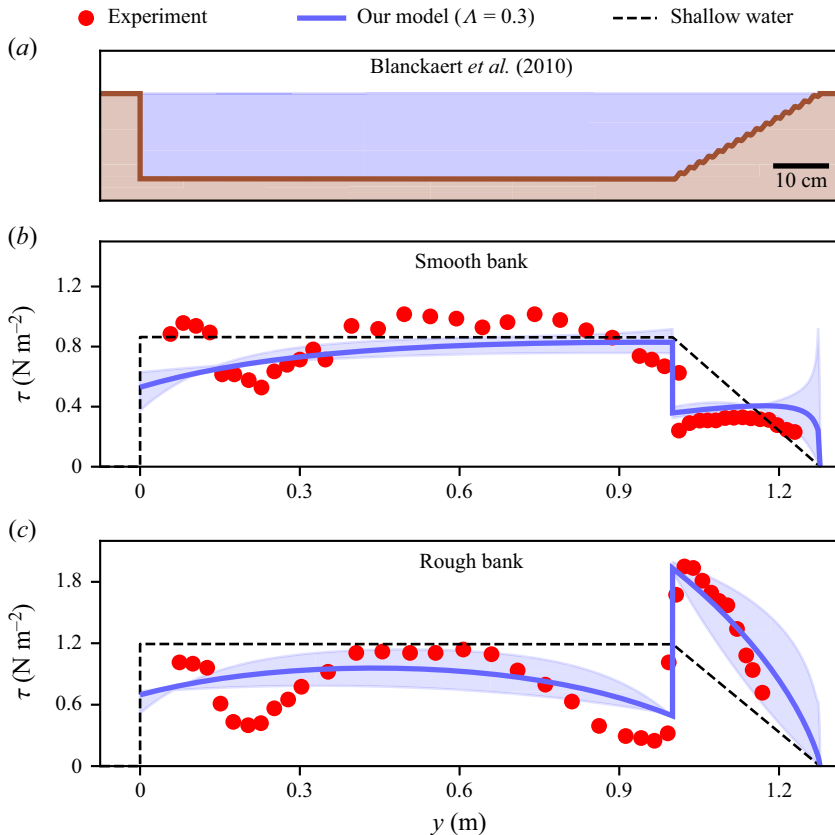
Figure 14. (*a*) A channel of Blanckaert *et al.* (2010) with a bank angle of 30°. Banks were coated with different material so that the bank roughness was less than, equal to or greater than the roughness of the flat bottom in different experiments. The friction coefficient is $C_f \approx 5.3 \times 10^{-3}$ on the bottom, while it varies on the banks. (*b*) Measurements (red circles) of the stress, τ, in the channel above with smooth banks. The blue line is the solution to (5.13) assuming default parameters $\Lambda = 0.3$, $\alpha = 0$ and $\theta = 0.8$ on the left vertical side wall, and C_f estimated using the Colebrook equation. The blue shading corresponds to the uncertainty in Λ and θ (table 2). The black dashed line corresponds to the shallow-water prediction. The downstream slope is $S \approx 5.5 \times 10^{-4}$. (*b*) A rough bank experiment. The notation is the same as above. The downstream slope is $S \approx 7.6 \times 10^{-4}$.

decreases, while a rough bank makes the stress exceptionally high on the bank, but, also, exceptionally low on the bottom near the junction point. We solve (5.13) using the default parameters ($\Lambda = 0.3$, $\alpha = 0$ and $\theta = 0.8$ on the left vertical side wall), and using the Colebrook equation (4.2) to estimate $C_f(y)$ as a function of the local Reynolds number approximated as $Re(y) = U_{sw}D(y)/\nu$ (where $U_{sw} = \sqrt{gSD(y)/C_{f,def}}$ and $C_{f,def} = 5.3 \times 10^{-3}$), and the relative roughness, $k_s(y)/R_h$, where $k_s(y)$ assumes different values on the bottom and the banks. This solution reproduces the measurements qualitatively well – it captures both the drop in the stress in the case of the smooth bank and its jump in the case of the rough bank. The value of Λ does not affect the magnitude of the jump in the stress – it only affects the shape of the stress curves. We find the best fit with $\Lambda \approx 0.18$ for the smooth bank experiment and $\Lambda \approx 0.31$ for the rough bank experiment, close to our default value.

Even though our model reproduces the measurements qualitatively well, there are still significant deviations. The measurements show strong variability around our solutions on scales comparable to the channel depth. This variability is of the same order as the deviation of our theory from the shallow-water prediction, and is, therefore, not negligible. It is likely that this is due to strong recirculation cells. This is an effect that we cannot hope to capture with our model on the scale of individual cells – our model can only give the stress smoothed out over several such cells.

6.5. *Summary of model parameters*

In summary, we find that our model reproduces most of the observations. The friction coefficient, C_f, is well captured by the Colebrook equation (4.2). The best-fit Λ varied from one experiment to another but was always of order one. The lowest best-fit value we found was $\Lambda = 0.07$ for the rectangular flume of Knight *et al.* (1984) with the smallest aspect ratio ($W/D \approx 2$), while the largest was $\Lambda \approx 1.05$ in the main channel of the floodplain experiment of Shiono & Knight (1991) with the smallest flow depth ($D_{mc} \approx 17$ cm). We chose our default value ($\Lambda = 0.3$) to be between these two extremes. Together with our estimates of C_f, this yields the diffusion parameter for the stress, $\chi = \Lambda C_f^{-1/2}$, between $\chi \approx 1.3$ and $\chi \approx 23.4$. The values of Λ we found here are compatible with previous estimates – Okoye (1970) tracked tracer dispersion in various experiments and field studies, and estimated the effective eddy diffusivity, $\mathcal{D}_e$, to be between $\mathcal{D}_e \approx 0.07 U^* D$ and $\mathcal{D}_e \approx 2.0 U^* D$. These measurements imply that our parameter $\Lambda = \mathcal{D}_e / 2 U^* D$ lies in the range between [0.03, 1.0], consistent with our present estimates.

Experimental evidence suggests that α is small – significant positive values of α lead to peaks in the stress that are not observed in the floodplain experiments of Shiono & Knight (1991), while significant negative values lead to an abrupt transition of the stress from the main channel to the floodplain which is, again, inconsistent with measurements. Theoretical arguments also suggest a small α for highly turbulent flows – the model of turbulent diffusion of Appendix A suggests that α decays logarithmically with the Reynolds number, as the velocity profile starts to resemble a vertically uniform 'plug' flow. For these reasons, we suggest the default value $\alpha = 0$ with a tentative uncertainty range around zero, $\alpha \in (-0.1, 0.1)$. Nevertheless, we note that care should be taken when dealing with flows at lower Reynolds numbers that do not resemble a 'plug' flow – approaching the laminar regime, the values of α should approach $\alpha = 1$.

In rectangular channels, it is necessary to prescribe a boundary condition, θ, at the vertical side wall. Measurements on the Seine suggest a no-slip boundary condition ($\theta \approx 0$) and do not support θ greater than $\theta \sim 0.1$. On the other hand, rectangular flume experiments suggest θ of order one. Depending on the experiment, the best-fit values range from $\theta \approx 0.6$ to $\theta \approx 1$, and we take the mid-value ($\theta = 0.8$) to be our default. We currently do not understand what causes this significant difference between the natural channel of the Seine and the experimental flumes.

Using $Re = 10^5$ and $C_f = 10^{-3}$ in the model of turbulent diffusion of Appendix A, we find $\Lambda \approx 0.03$ and $\alpha \approx 0.17$ (A11*a*,*b*). The value of Λ in this model is lower than our observed values, while the value of α is too large to be supported by the data. This suggests that, although the model of turbulent diffusion captures many qualitative features of turbulent momentum transfer, it is not quantitatively accurate. We note that $\Lambda \approx 0.03$ corresponds to the lowest value measured by Okoye (1970), who hypothesised that this is the theoretical lower bound.

981 A24-28

6.6. *Validity of model assumptions in the experiments*

We derived our model under four assumptions: (i) the transfer of momentum across the stream does not depend on the gravity, g, viscosity, ν, and the bed roughness, k_s; (ii) the vertical profile of velocity does not change shape across the stream; (iii) the flux of momentum, F, is locally related to the flow depth and velocity; and (iv) the depth and velocity vary slowly across the stream. None of these assumptions were exactly satisfied in the experiments we considered.

The flux in our model depends on the Reynolds number and the bed roughness through the friction coefficient, although it does so only weakly. This violates the first assumption of our model, and we partly took it into account by allowing C_f to vary according to the Colebrook equation.

Chauvet (2014) measured the vertical profiles of velocity at different locations in the Seine. Based on their measurements, we estimate that the contribution to the flux, F, due to the changing shape of the vertical velocity profile is likely more than an order of magnitude smaller than the contribution due to the velocity gradient, $U\tilde{\sigma}'_U/U' \sim 0.04$, where $\tilde{\sigma}_U = \sigma_U/U$ is the dimensionless standard deviation of the velocity profile that characterises its shape. This is consistent with our second assumption above, but we note that variations of the profile's shape likely become significant near the corners where the bed intersects the free surface, especially when $\alpha > 0$ and our model diverges (§ 5.3).

The non-local contributions to the flux generated two notable features in the data that we could not reproduce: (i) the large fluctuations of the stress in the experiments of Blanckaert *et al.* (2010) on the scale of the flow depth, probably related to recirculation cells; and (ii) the slight but consistent underestimate of the stress in the floodplain region in the experiments of Shiono & Knight (1991), possibly caused by large, horizontal eddies or recirculation cells. These features contributed to about 20 % error in our model, but they may become weaker in natural, irregular channels with a rough bed (Blanckaert *et al.* 2010).

Finally, none of the experiments we considered really had a slowly varying topography throughout the channel – they all contained sharp corners or steep banks. The fact that the experiments of Shiono & Knight (1991) had banks with $D' = 1$, means that the higher-order terms in the flux (for example, those proportional to D'^2) are of a similar order of magnitude to the one we considered. This could explain why our model produced a small peak of the stress between the main channel and the floodplain, which was not observed by Shiono & Knight (1991).

Despite these inconsistencies, most of the data fell within the uncertainty bounds of our model, while our default parameters (table 2) reproduced the data to within about 30 %. Our model always provided a significant improvement to the shallow-water approximation. The data we considered cover about three orders of magnitude in Reynolds number (from about 10^4 for some rectangular flumes to about 7×10^6 for the Seine), and include channels of varying shape with a smooth or rough bed, as well as those with variable roughness. These reasons suggest that the model we presented here is reasonable.

7. Conclusions

In this paper we explored in detail a model for the steady-state distribution of the stress generated by a turbulent flow in a straight channel with an arbitrary, albeit slowly varying, bottom topography. This model is a simple linear, ODE for the stress that assumes that eddies and recirculation cells of a size comparable to the channel depth carry most of the momentum across the stream. It assumes that the flow depth and velocity vary slowly

relative to the size of the dominant eddies or recirculation cells – in this case, momentum transfer across the stream becomes diffusive, driven by simple gradients of time-averaged velocity.

Our model contains two dimensionless parameters – the diffusion parameter for the stress, χ, equal to about the ratio of the dominant eddy velocity to the downstream velocity, and the local-shape parameter, α, which arises due to horizontal velocity gradients induced by the variation of the flow depth. Assuming that dominant eddies move at roughly the frictional velocity, we estimated that the diffusion parameter is of the order of the inverse square root of the friction coefficient, $\chi = \Lambda C_f^{-1/2}$. On the other hand, assuming a homogeneous turbulence, we suggested the local-shape parameter, α, vanishes as the flow becomes more and more turbulent and the vertical profile of velocity becomes close to uniform. When comparing our model to various experimental and natural flows, we found that $\Lambda = 0.3$ and $\alpha = 0$ reproduced all of these diverse measurements to within about 30 %.

This model follows from dimensional analysis under generic assumptions about the flow, such as the locality of the cross-stream flux of momentum and the fixed shape of the vertical velocity profile. As a first-order, diffusive approximation, it is equally valid for turbulent and laminar flows (which is obtained by setting the parameters to $\alpha = 1$ and $\chi = 1/3$). This suggests that it may be possible to describe other types of flows, such as the non-Newtonian flow of ice, by simply adjusting these parameters.

We developed this model with natural rivers in mind. As was proposed by Parker (1978*b*), and demonstrated experimentally by Popović *et al.* (2021) in the case of laminar laboratory rivers, the transfer of momentum across the stream is crucial to the stability of an alluvial river that transports sediment. The present model suggests that it may be possible to understand equilibrium shape of alluvial, turbulent rivers as simply as in laminar ones, at least to first order.

Declaration of interests. The authors report no conflict of interest.

Author ORCIDs.

Predrag Popović https://orcid.org/0000-0001-7937-9153;

Olivier Devauchelle https://orcid.org/0000-0002-7295-4896;

Eric Lajeunesse https://orcid.org/0000-0002-0950-6054.

Appendix A. Turbulent diffusion

In this section we show how (3.7) arises explicitly in a specific model of turbulent diffusion. We use this to demonstrate how our heuristic arguments work in practice, and calculate the parameters Λ and α.

In the model of turbulent diffusion, like in a laminar flow, the momentum diffuses at a rate proportional to the local velocity gradient, $\rho \mathcal{D}_e \nabla u$. Unlike the molecular viscosity, however, the turbulent diffusivity, $\mathcal{D}_e$, varies throughout the flow because the properties of the eddies that carry the momentum differ near a channel's bottom and far away from it – $\mathcal{D}_e$ is generally highest near the centre of the flow, where the turbulent eddies are the largest and move at the greatest velocities. Over a flat surface, the turbulent diffusivity, $\mathcal{D}_e$, usually develops a parabolic vertical profile that vanishes at the bottom and at the surface (Nezu & Nakagawa 1993):

$$\mathcal{D}_e = -\mathcal{D}_0 \frac{z}{D} \left(1 + \frac{z}{D} \right). \tag{A1}$$

Here $\mathcal{D}_0$ is the turbulent diffusivity scale, and the minus sign ensures that the diffusivity is positive ($z \leq 0$). Empirical studies show that the turbulent diffusivity scale is about (Nezu & Nakagawa 1993)

$$\mathcal{D}_0 \approx \kappa U^* D, \tag{A2}$$

where $\kappa \approx 0.4$ is the von Kármán constant and U^* is the frictional velocity. Equation (A2) reflects our remark in § 3.1 that turbulent diffusivity is proportional to the size (of the order of D) and to the velocity (of the order of U^*) of the largest eddies. For highly turbulent flows, the parabolic diffusivity profile (A1) corresponds to a logarithmic velocity profile (Schlichting & Gersten 2000)

$$u^+ = \frac{1}{\kappa} \ln z^+ + C^+, \tag{A3}$$

where $u^+ \equiv u(z)/U^*$ is the dimensionless velocity, $z^+ \equiv (D + z)U^*/\nu$ is the dimensionless vertical coordinate and C^+ is a constant equal to $C^+ \approx 5$ in channels with smooth walls. The flow is fully turbulent when $z^+ \gtrsim 70$, while for $z^+ \lesssim 5$, it is laminar. Typically, there also exists an 'outer-layer wake' near the free surface where the velocity deviates from the logarithmic law of (A3). Here, we neglect the part of the flow below the turbulent layer (for $z^+ \lesssim 70$) as well as the outer-layer wake. We consider that the dimensionless depth is much greater than one, $D^+ \equiv DU^*/\nu \gg 1$, but we will not immediately ignore the terms proportional to its logarithm, $\ln D^+$.

We can find the turbulent diffusive flux of momentum, F, in this approximation by integrating $\rho \mathcal{D}_e \nabla u$ over a vertical slice:

$$F = -\rho \int_{-D+z_0^+ \nu/U^*}^{0} \mathcal{D}_e \frac{\partial u}{\partial y} \, \mathrm{d}z. \tag{A4}$$

Here $z_0^+ \approx 70$ is the value of z^+ at the lower end of the turbulent layer. Using the diffusivity and velocity profiles of (A1) and (A3), neglecting terms of order $1/D^+$ but retaining those proportional to $\ln D^+$, and after a considerable amount of straightforward algebra, we find the flux in (A4):

$$F = -\rho \mathcal{D}_0 \left[U'D\mathcal{I}_1 + UD'\mathcal{I}_2 \right]. \tag{A5}$$

Here, in the limit we are considering ($D^+ \gg 1$ and $\ln(D^+) \sim 10$), the prefactors $\mathcal{I}_1$ and $\mathcal{I}_2$ are

$$\mathcal{I}_1 = \frac{1}{6} - \frac{5}{36 \left(\ln D^+ + \kappa C^+ \right)} + O\left(\frac{1}{D^+} \right), \tag{A6}$$

$$\mathcal{I}_2 = \frac{1}{3 \left(\ln D^+ + \kappa C^+ \right)} + \frac{5}{36 \left(\ln D^+ + \kappa C^+ \right)^2} + O\left(\frac{1}{D^+} \right). \tag{A7}$$

The terms U' and D' both arise from taking the cross-stream derivative of the velocity, $\partial u/\partial y$. Expressing the frictional velocity as $U^* = C_f^{1/2} U$, we find the diffusivity scale

$\mathcal{D}_0 = \kappa C_f^{1/2} U D$. Using this and reorganising the terms in (A5), we get

$$F = -\rho C_f^{1/2} \Lambda \big[(U^2)' D^2 + \alpha U^2 (D^2)'\big], \qquad (A8)$$

where the diffusion parameter, Λ, and the local-shape parameter, α, are

$$\Lambda = \frac{\kappa}{12}\left(1 - \frac{5}{6\left(\ln D^+ + \kappa C^+\right)}\right) + O\left(\frac{1}{D^+}\right), \qquad (A9)$$

$$\alpha = \frac{2}{\ln D^+ + \kappa C^+}\,\frac{\ln D^+ + \kappa C^+ - 5/12}{\ln D^+ + \kappa C^+ - 10/12} + O\left(\frac{1}{D^+}\right). \qquad (A10)$$

We thus find the expression 3.7 for the flux, F, in this model of turbulent diffusion. For highly turbulent fluids, the logarithms $\ln D^+$ also become large, so, to leading order in large $\ln D^+$, we find that

$$\Lambda \approx \frac{\kappa}{12}, \quad \alpha \approx \frac{2}{\ln\left(Re C_f^{1/2}\right)}, \qquad (A11a,b)$$

where we used $U^* = C_f^{1/2} U$ to express $D^+ = Re C_f^{1/2}$. Therefore, Λ is a constant of order one ($\Lambda \approx 0.03$), while α vanishes logarithmically with the Reynolds number.

Equation (A8) holds in the model of turbulent diffusion for any shape of vertical profiles of velocity and diffusivity so long as the diffusivity scales as $\mathcal{D}_e \propto UD$ – logarithmic velocity and parabolic diffusivity are not necessary. Different profiles of velocity and diffusivity only change the values of Λ and α. The value of α only depends on the shapes of these profiles, while the value of Λ also depends on the scale of the diffusivity, $\mathcal{D}_0/(U^*D)$. A vertically uniform velocity leads to $\alpha = 0$ regardless of the diffusivity, while $\alpha < 0$ can occur only if the flow near the bottom is faster than the flow near the surface.

Appendix B. Local model

Even though we assumed that the flux, F, is locally related to the depth and the velocity, the stress, τ, resulting from (4.6) is non-local – at each point, it depends on the entire shape of the channel. In this appendix, we derive a 'local' approximation for the stress, τ, in which it is related directly to the local depth and its derivatives. In this approximation, there is no need to solve the full (4.6), but the approximation is only meaningful for small enough values of the diffusion parameter, χ.

In this approximation we assume that the variations in the depth are slow compared with the depth itself so that $\tilde{D}' \sim \epsilon \ll \tilde{D}$, where ϵ is a small parameter of the order of the inverse of the aspect ratio, $\epsilon \sim D_{max}/W$. Then, we assume that $\tilde{\tau}$ can be expanded in a series as

$$\tilde{\tau}(\tilde{y}) = \tilde{\tau}^{(0)}(\tilde{y}) + \tilde{\tau}^{(1)}(\tilde{y}) + \cdots, \qquad (B1)$$

where the nth-order term is of the order ϵ^n. The zeroth order in this expansion assumes that there are no variations in the depth, $\tilde{D}' = 0$, so that it corresponds to the shallow-water stress, $\tilde{\tau}^{(0)} = \tilde{D}$. We then insert this zeroth-order stress into the expression for the flux,

981 A24-32

$\tilde{F} = -\chi(\tilde{D}^2\tilde{\tau}' + \alpha\tilde{\tau}(\tilde{D}^2)')$, to get the flux to the first non-trivial order:

$$\tilde{F}^{(1)} \approx -\frac{\chi(2\alpha+1)}{3}(\tilde{D}^3)'. \tag{B2}$$

The superscipt (1) in the flux signifies that the first non-vanishing order of the flux is of the order of ϵ (i.e. proportional to $\tilde{D}'$). The flux at the zeroth order corresponds to the shallow-water approximation, and, therefore, vanishes. If we use (B2) for the flux in the momentum balance (2.3), we can find the stress corrected to the next order in the expansion

$$\tilde{\tau} \approx \left(\tilde{D} + \frac{\chi(2\alpha+1)}{3}\left(\tilde{D}^3\right)''\right)\cos\phi, \tag{B3}$$

where $\cos\phi = (1 + \tilde{D}'^2)^{-1/2}$. This is the stress corrected up to the order ϵ^2. It is the first order that contains a non-trivial contribution from the cross-stream transfer of momentum. Inserting this expression for the stress back into the flux, we can also get higher-order corrections for $\tilde{F}$, which, through (2.3), yield higher-order corrections for $\tilde{\tau}$.

In (B3) the stress at a point $\tilde{y}$ is only related to the local depth, $\tilde{D}(\tilde{y})$, and its first two derivatives at that point. In this way, we do not need to know the entire shape of the channel in order to find the stress at a particular point. Although we can follow the procedure above to find the stress to an arbitrarily high order, all of these corrections remain local – for example, we will never be able to capture the effects of vertical side walls in a rectangular channel in this way, no matter the order to which we approximate the stress.

In some applications, this local approximation may suffice. Notably, Popović *et al.* (2021) showed that a similar approximation was sufficient to explain the shape of laminar laboratory rivers that carry sediment. This may not always be the case if the variations in the depth are too great or if the diffusion parameter for the stress, χ, is too large – the expansion in terms of small ϵ (B1) may not exist. In Appendix C we demonstrate a transition from a local stress to a non-local one near a corner for high enough values of χ (C5). In fact, (C5) likely also serves as a rule of thumb for when we can use the local approximation (B3). If the gradient of the topography is too large or the momentum diffusion is too strong, we need to solve the full (4.6) in order to get a meaningful approximation of the stress.

Appendix C. Corner flow

In this appendix we derive the equation for the flow along a corner, which can be used to construct the solutions to our model in a triangular channel (§ 5.3). In doing this, we show two features of our model: (i) the transition from a local to a non-local flow for high values of the diffusion parameter, χ; and (ii) the breakdown of our model for high enough values of χ when α is positive. This section also demonstrates how convenient it is that our model, (4.6), is linear in $\tilde{\tau}$.

We consider a bed that slopes downwards at an angle ϕ with the horizontal, starting from a corner at $\tilde{y} = 0$. The depth, therefore, increases as

$$\tilde{D} = \tilde{y}\tan\phi. \tag{C1}$$

This depth profile lacks a boundary condition on the open end of the corner, so we cannot fully solve (4.6) for the stress. Nevertheless, we can find $\tilde{\tau}$ up to an integration constant.

Since (4.6) is linear in $\tilde{\tau}$, we can write its solution as a sum of a particular and a homogeneous solution, $\tilde{\tau} = \tilde{\tau}_p + \tilde{\tau}_h$. The particular solution is proportional to the depth,

$$\tilde{\tau}_p = \frac{\tilde{D}}{\sqrt{1 + (\tan\phi)^2 - 2(2\alpha + 1)\chi \, (\tan\phi)^2}}. \tag{C2}$$

On the other hand, we can find the homogeneous solution in the form of a power law:

$$\tilde{\tau}_h = A\tilde{D}^a. \tag{C3}$$

Here A is an integration constant that depends on the entire shape of the channel, and the exponent, a, is

$$a = -\frac{2\alpha + 1}{2} + \sqrt{\frac{(1 - 2\alpha)^2}{4} + \frac{\sqrt{1 + (\tan\phi)^2}}{\chi \, (\tan\phi)^2}}. \tag{C4}$$

The particular solution is proportional to the depth and is independent of the shape of the bed beyond the corner. In this sense, it is local – the stress depends only on the local depth. On the other hand, the homogeneous solution is non-local – it depends on the entire channel beyond the corner through the constant A. Which one of these two solutions dominates near the corner depends on whether the exponent, a, is less than or greater than one. When a is less than one, the homogeneous solution takes over near the corner, and the flow feels the entire shape of the channel. This happens when the momentum transfer is strong enough:

$$a < 1 \quad \Longleftrightarrow \quad \chi > \frac{\sqrt{1 + (\tan\phi)^2}}{2(2\alpha + 1) \, (\tan\phi)^2}. \tag{C5}$$

Thus, (C5) defines a threshold diffusion parameter, χ, or a threshold channel slope, ϕ, beyond which the flow near the corner transitions from local to non-local.

If we keep increasing the intensity of the momentum transfer, the exponent of the homogeneous solution, a, can become negative:

$$a < 0 \quad \Longleftrightarrow \quad \chi > \frac{\sqrt{1 + (\tan\phi)^2}}{2\alpha \, (\tan\phi)^2}. \tag{C6}$$

When this happens, the homogeneous solution diverges near the corner, leading to an unphysical situation. Therefore, we may say that $a < 0$ represents the point at which our theory breaks down. By noting that $\tan\phi = 2D_{max}/W$, and solving for $\tan\phi$ in (C6), we retrieve (5.12) of § 5.3.

If we specify the full shape of the channel, we can find the integration constant, A. In a triangular channel of figure 9(a), the depth profile is given by

$$\tilde{D} = \begin{cases} \tilde{y}\tan\phi & \text{if } \tilde{y} \leq \dfrac{\tilde{W}}{2}, \\[2mm] (\tilde{W} - \tilde{y})\tan\phi & \text{if } \tilde{y} > \dfrac{\tilde{W}}{2}. \end{cases} \tag{C7}$$

In both halves of the channel the solution is given by the same sum of the particular and homogeneous solution we just discussed, so we simply need to determine the constant, A.

981 A24-34

To find it, we assume that the stress, τ, and the flux, F, are continuous at the junction between the two halves (in fact, due to symmetry, the flux at this point vanishes). This yields

$$A = \frac{\tilde{D}_{max}^{1-a}}{(2\alpha + a)(2\chi (\tan \phi)^2 - \sqrt{1 + (\tan \phi)^2}/(2\alpha + 1))}. \tag{C8}$$

These solutions are shown in figure 9(b,c).

C.1. *Poisson equation*

To find the unapproximated laminar stress in the triangular channel of figure 9 (red dotted line in figure 9), we solve the Poisson equation for the velocity,

$$\frac{\partial^2 \tilde{u}}{\partial \tilde{y}^2} + \frac{\partial^2 \tilde{u}}{\partial \tilde{z}^2} = -1, \tag{C9}$$

with a no-slip boundary condition at the bed, $\tilde{u}(\tilde{z} = -\tilde{D}) = 0$. Since this equation is linear, the resulting velocity is the sum of the particular and the homogeneous solution, $\tilde{u} = \tilde{u}_p + \tilde{u}_h$. For the corner of (C1), the particular solution is

$$\tilde{u}_p = \frac{(\tilde{y} \tan \phi)^2 - \tilde{z}^2}{2(1 - \tan^2 \phi)}. \tag{C10}$$

A homogeneous solution is (Polubarinova-Kochina 1962)

$$\tilde{u}_h = C_n Re\left(\omega^{(2n+1)(\pi/2\phi)}\right) \tag{C11}$$

for any integer $n > 0$. Here, $\omega = \tilde{y} + i\tilde{z}$ is a complex combination of the coordinates, $Re(\cdots)$ stands for the real part and C_n is a constant. Therefore, the full solution, $\tilde{u}$, is

$$\tilde{u}(\tilde{y}, \tilde{z}) = \frac{(\tilde{y} \tan \phi)^2 - \tilde{z}^2}{2(1 - \tan^2 \phi)} + \sum_{n=1}^{\infty} C_n Re(\omega^{(2n+1)(\pi/2\phi)}), \tag{C12}$$

where C_n are constants to be determined from the boundary condition at the centre of the triangular channel. Due to the symmetry of the channel, the velocity gradient must vanish at the centre, $\partial \tilde{u}/\partial \tilde{y}|_{\tilde{y}=\tilde{W}/2} = 0$. By considering this condition at N distinct heights, $\tilde{z}_1, \ldots, \tilde{z}_N$, we can find the constants C_n to arbitrary order N (the solution in figure 9 assumes $N = 50$). After determining the constants C_n, we find the components of the stress as $\tilde{\tau}_z = \partial \tilde{u}/\partial \tilde{z}|_{\tilde{z}=-\tilde{D}}$ and $\tilde{\tau}_y = \partial \tilde{u}/\partial \tilde{y}|_{\tilde{z}=-\tilde{D}}$, and the total stress as $\tilde{\tau} = (\tilde{\tau}_z^2 + \tilde{\tau}_y^2)^{1/2}$.

Appendix D. Details about the experiments

In this appendix we give the details of the experiments we compared our model with. All of these details can be found in the cited references, but we give them here for the reader's convenience.

D.1. *Chauvet et al. (2014)*

In the Paris region, the Seine river flows down a gentle slope of about $S \approx 10^{-4}$, with a Reynolds number of about $Re \approx 7 \times 10^{6}$. At the time and the location at which Chauvet *et al.* (2014) took their measurements, it was about 148 m wide and about 6.2 m deep. Their measurements were based on readings from an acoustic doppler current profiler fixed to a raft that was tethered to a footbridge, and shifted across the flow.

D.2. *Knight et al. (1984)*

Knight *et al.* (1984) performed a series of experiments in smooth rectangular channels whose width varied between $W = 7$ cm and $W = 61$ cm. The slope in all experiments was fixed at $S = 9.66 \times 10^{-4}$, while the flow depth was varied by adjusting the water discharge. The resulting aspect ratio varied between 0.31 and 19.12, with a Reynolds number varying between about 10^{4} and 7×10^{4}. They measured the stress with a Preston tube method (Preston 1954).

D.3. *Shiono & Knight (1991)*

Shiono & Knight (1991) investigated the flow and the stress distribution in idealised experiments that resemble a river with a floodplain (figure 13). Their channels consisted of a deep main channel of width $W_{mc} = 1.5$ m, surrounded by two shallow parts (the 'floodplain'), each $W_{fp} = 2.25$ m wide. The water level changed from one experiment to the next, so that the depth of the main channel varied between $D_{mc} = 15$ cm and $D_{mc} = 30$ cm, and that of the floodplain between $D_{fp} = 0$ and $D_{fp} = 15$ cm. The difference between the two depths was fixed by experimental design at $D_{mc} - D_{fp} = 15$ cm. The downstream slope of the channel was fixed at $S = 1.027 \times 10^{-3}$. Shiono & Knight (1991) measured the velocity using a two-channel laser doppler anemometer across one half of the channel. They measured the stress across the channel using Preston tubes (Preston 1954). The velocities were about 1 m s^{-1}, which yields a Reynolds number of about 3×10^{5}, similar to the largest experiments considered by Knight *et al.* (1984), and about an order of magnitude lower than in the Seine.

D.4. *Blanckaert et al. (2010)*

The experiments of Blanckaert *et al.* (2010) were performed in half-trapezoidal channels, such as the one shown in figure 14. The left bank was a vertical wall, whereas the right bank had a slope of either $30°$ or $45°$, depending on the experiment. The width of the flat bottom was about $W_{bot} = 1.2$ m, the flow depth about $D_{bot} = 16$ cm, the flow speed about $U \sim 0.4$ m s^{-1} and the Reynolds number about $Re \sim 7 \times 10^{4}$. The bottom of the channel was roughened by gluing beads of size $k_{s,bot} = 2$ mm. They considered three cases for the banks: smooth banks ($k_{s,bank} \approx 0$), banks that were as rough as the bottom ($k_{s,bank} = 2$ mm) and rough banks ($k_{s,bank} = 30$ mm). Unlike Shiono & Knight (1991), Blanckaert *et al.* (2010) did not measure the stress directly, but estimated it from the vertical velocity profiles.

REFERENCES

ABRAMIAN, A., DEVAUCHELLE, O. & LAJEUNESSE, E. 2019 Streamwise streaks induced by bedload diffusion. *J. Fluid Mech.* **863**, 601–619.

ABRAMIAN, A., DEVAUCHELLE, O. & LAJEUNESSE, E. 2020 Laboratory rivers adjust their shape to sediment transport. *Phys. Rev.* E **102** (5), 053101.

BARENBLATT, G.I. 1996 *Scaling, Self-Similarity, and Intermediate Asymptotics: Dimensional Analysis and Intermediate Asymptotics*. Cambridge University Press.

BATCHELOR, G.K. 1967 *An Introduction to Fluid Dynamics*. Cambridge University Press.

BLANCKAERT, K., DUARTE, A. & SCHLEISS, A.J. 2010 Influence of shallowness, bank inclination and bank roughness on the variability of flow patterns and boundary shear stress due to secondary currents in straight open-channels. *Adv. Water Resour.* **33** (9), 1062–1074.

BOUCHEZ, J., LAJEUNESSE, E., GAILLARDET, J., FRANCE-LANORD, C., DUTRA-MAIA, P. & MAURICE, L. 2010 Turbulent mixing in the Amazon river: the isotopic memory of confluences. *Earth Planet. Sci. Lett.* **290** (1–2), 37–43.

BOUSMAR, D. & ZECH, Y. 1999 Momentum transfer for practical flow computation in compound channels. *ASCE J. Hydraul. Engng* **125** (7), 696–706.

CHAUVET, H. 2014 Écoulements secondaires dans les rivières: influence sur le transport de quantité de mouvement et de soluté. PhD thesis, Université Paris-Diderot-Paris VII.

CHAUVET, H., DEVAUCHELLE, O., MÉTIVIER, F., LAJEUNESSE, E. & LIMARE, A. 2014 Recirculation cells in a wide channel. *Phys. Fluids* **26** (1), 016604.

CHÉZY, A. 1775 Memoire sur la vitesse de l'eau conduit dans une rigole donne. *Dossier* **847**, 363–368.

CHOW, V.T. 1959 *Open Channel Hydraulics*. McGraw-Hill.

COLEBROOK, C.F. 1939 Turbulent flow in pipes, with particular reference to the transition region between the smooth and rough pipe laws. *J. Inst. Civil Engrs* **11**, 133–156.

CRUFF, R.W. 1965 *Cross-Channel Transfer of Linear Momentum in Smooth Rectangular Channels*. US Government Printing Office.

DEVAUCHELLE, O., POPOVIĆ, P. & LAJEUNESSE, E. 2022 Viscous transfer of momentum across a shallow laminar flow. *J. Fluid Mech.* **932**, A32.

ECHELMEYER, K.A., HARRISON, W.D., LARSEN, C. & MITCHELL, J.E. 1994 The role of the margins in the dynamics of an active ice stream. *J. Glaciol.* **40** (136), 527–538.

GHOSH, S.N. & ROY, N. 1970 Boundary shear distribution in open channel flow. *J. Hydraul. Div. ASCE* **96** (4), 967–994.

GIOIA, G. & BOMBARDELLI, F.A. 2001 Scaling and similarity in rough channel flows. *Phys. Rev. Lett.* **88** (1), 014501.

GIOIA, G. & CHAKRABORTY, P. 2006 Turbulent friction in rough pipes and the energy spectrum of the phenomenological theory. *Phys. Rev. Lett.* **96** (4), 044502.

GIOIA, G., GUTTENBERG, N., GOLDENFELD, N. & CHAKRABORTY, P. 2010 Spectral theory of the turbulent mean-velocity profile. *Phys. Rev. Lett.* **105** (18), 184501.

GLOVER, R.E. & FLOREY, Q.L. 1951 Stable channel profiles. Hydraulic laboratory report HYD. U.S. Department of the Interior, Bureau of Reclamation, Design and Construction Division.

KADDI, Y., CIERCO, F.-X., FAURE, J.-B. & PROUST, S. 2022 New developments in a 1D+ ISM model for operational purposes. In *Advances in Hydroinformatics: Models for Complex and Global Water Issues—Practices and Expectations* (ed. P. Gourbesville & G. Caignaert), pp. 61–83. Springer.

KARTHA, V.C. & LEUTHEUSSER, H.J. 1970 Distribution of tractive force in open channels. *J. Hydraul. Div. ASCE* **96** (7), 1469–1483.

KNIGHT, D.W., DEMETRIOU, J.D. & HAMED, M.E. 1984 Boundary shear in smooth rectangular channels. *ASCE J. Hydraul. Engng* **110** (4), 405–422.

KNIGHT, D.W. & MACDONALD, J.A. 1979 Hydraulic resistance of artificial strip roughness. *J. Hydraul. Div.* **105** (6), 675–690.

LAJEUNESSE, E., MALVERTI, L. & CHARRU, F. 2010a Bed load transport in turbulent flow at the grain scale: experiments and modeling. *J. Geophys. Res.* **115**, F04001.

LAJEUNESSE, E., MALVERTI, L., LANCIEN, P., ARMSTRONG, L., METIVIER, F., COLEMAN, S., SMITH, C.E., DAVIES, T., CANTELLI, A. & PARKER, G. 2010b Fluvial and submarine morphodynamics of laminar and near-laminar flows: a synthesis. *Sedimentology* **57** (1), 1–26.

MALVERTI, L., LAJEUNESSE, E. & MÉTIVIER, F. 2008 Small is beautiful: upscaling from microscale laminar to natural turbulent rivers. *J. Geophys. Res.* **113**, F04004.

MARTIN-VIDE, J.P. & MORETA, P.J.M. 2008 Formulae for apparent shear stress in straight compound channels with smooth floodplains. In *River Flow 2008: Proceedings of the International Conference on Fluvial Hydraulics Cesme-Izmir, Turkey, 3–5 September 2008* (ed. M.S. Altnaker, M.A. Kokpinar, I. Aydin, S. Cokgar & S. Kirkgoz), pp. 465–476. Kubaba Congress Department and Travel Services.

MÉTIVIER, F. & BARRIER, L. 2012 Alluvial landscape evolution: What do we know about metamorphosis of gravel-bed meandering and braided streams? In *Gravel-bed Rivers: Processes, Tools, Environments* (ed. M. Church, P.M. Biron & A.G. Roy), pp. 474–501. Wiley.

MÉTIVIER, F., *et al.* 2016 Geometry of meandering and braided gravel-bed threads from the Bayanbulak Grassland, Tianshan, PR China. *Earth Surf. Dyn.* **4** (1), 273–283.

MYERS, W.R.C. 1978 Momentum transfer in a compound channel. *J. Hydraul. Res.* **16** (2), 139–150.

NEZU, I. & NAKAGAWA, H. 1993 *Turbulence in Open-Channel Flows*. Balkema.

NIKURADSE, J. 1933 Stromungsgesetze in rauhen rohren. *VDI-Forsch.* **361**, 1.

NOUTSOPOULOS, G.C. & HADJIPANOS, P.A. 1982 Discussion of "boundary shear in smooth and rough channels". *J. Hydraul. Div. ASCE* **108** (6), 809–812.

OKOYE, J.K. 1970 Characteristics of transverse mixing in open channel flows. *Tech. Rep.* KH.

PARKER, G. 1978*a* Self-formed straight rivers with equilibrium banks and mobile bed. Part 1. The sand-silt river. *J. Fluid Mech.* **89** (1), 109–125.

PARKER, G. 1978*b* Self-formed straight rivers with equilibrium banks and mobile bed. Part 2. The gravel river. *J. Fluid Mech.* **89** (1), 127–146.

POLUBARINOVA-KOCHINA, P.Y. 1962 *Theory of Ground Water Movement*. Princeton University Press.

POPE, S.B. 2011 Simple models of turbulent flows. *Phys. Fluids* **23** (1), 011301.

POPOVIĆ, P., DEVAUCHELLE, O., ABRAMIAN, A. & LAJEUNESSE, E. 2021 Sediment load determines the shape of rivers. *Proc. Natl Acad. Sci.* **118** (49), e2111215118.

PRANDTL, L. 1925 Bericht über untersuchungen zur ausgebildeten turbulenz. *Z. Angew. Math. Mech.* **5** (2), 136–139.

PRESTON, J.H. 1954 The determination of turbulent skin friction by means of pitot tubes. *Aeronaut. J.* **58** (518), 109–121.

PROUST, S., BOUSMAR, D., RIVIERE, N., PAQUIER, A. & ZECH, Y. 2009 Nonuniform flow in compound channel: a 1-D method for assessing water level and discharge distribution. *Water Resour. Res.* **45** (12), W12411.

RICHARDSON, L.F. 1920 The supply of energy from and to atmospheric eddies. *Proc. R. Soc. Lond.* A **97** (686), 354–373.

RODBARD, S. 1975 Vascular caliber. *Cardiology* **60** (1), 4–49.

SAMUELS, P.G. 1985 Modelling of river and flood plain flow using the finite element method. Report no. SR61. Hydraulics Research Laboratory.

SCHLICHTING, H. & GERSTEN, K. 2000 *Boundary-Layer Theory*, 8th edn. Springer.

SEIZILLES, G., DEVAUCHELLE, O., LAJEUNESSE, E. & MÉTIVIER, F. 2013 Width of laminar laboratory rivers. *Phys. Rev.* E **87** (5), 052204.

SHIH, H.-Y., HSIEH, T.-L. & GOLDENFELD, N. 2016 Ecological collapse and the emergence of travelling waves at the onset of shear turbulence. *Nat. Phys.* **12** (3), 245–248.

SHIONO, K. & KNIGHT, D.W. 1991 Turbulent open-channel flows with variable depth across the channel. *J. Fluid Mech.* **222**, 617–646.

TAYLOR, G.I. 1935 Statistical theory of turbulenc. *Proc. R. Soc. Lond.* A **151** (873), 421–444.

TOMINAGA, A., NEZU, I., EZAKI, K. & NAKAGAWA, H. 1989 Three-dimensional turbulent structure in straight open channel flows. *J. Hydraul. Res.* **27** (1), 149–173.

WARK, J.B., SAMUELS, P.G. & ERVINE, D.A. 1990 A practical method of estimating velocity and discharge in compound channels. In *River Flood Hydraulics* (ed. W.R. White), pp. 163–172. Wiley.

ZNAIEN, J., HALLEZ, Y., MOISY, F., MAGNAUDET, J., HULIN, J.-P., SALIN, D. & HINCH, E.J. 2009 Experimental and numerical investigations of flow structure and momentum transport in a turbulent buoyancy-driven flow inside a tilted tube. *Phys. Fluids* **21** (11), 115102.